Hardin, R.A., and Beckermann, C., "Measurement and Prediction of Mechanical Behavior of Cast Steel Plates with Centerline Porosity," in Proceedings of the 65th SFSA Technical and Operating Conference, Paper No. 5.4, Steel Founders' Society of America, Chicago, IL, 2011.

Measurement and Prediction of Mechanical Behavior of Cast Steel Plates with Centerline Porosity

Richard A. Hardin and Christoph Beckermann

Department of Mechanical and Industrial Engineering
The University of Iowa, Iowa City, IA 52242

Abstract

Tensile test plates were machined from normalized and tempered WCB steel castings. The casting geometries were designed such that feeding distances were exceeded and centerline shrinkage formed. The test plates were radiographed, and the radiographs were used to determine the quantitative amount of porosity in the plates. The ASTM RT Levels of all plates were 4 to 5. It was found that the stiffness of the plate castings ranged from 72% to 95% of sound material, with an average of 88% of sound material. The yield stress was not reduced on average for the tensile test plates, and ranged from 92% to 109% of the sound yield stress. The ultimate tensile strength also changed little from the sound material. Ductility in the test castings was markedly reduced with the percent elongation data ranging from 12.8% to 19.6%; versus 22% elongation measured in the sound material. The radiographs of the test plates were used to generate centerline porosity in a stress analysis model. The porous metal plasticity model in the *ABAQUS* finite element stress analysis software was used to predict the tensile curves of the castings with porosity and their failure. Agreement was excellent in some cases with the measured tensile curves and the observed failure location. Ductility (elongation) predictions were good and conservative.

I. INTRODUCTION

Carbon steels, such as ASTM A216 Grade WCB, exhibit a combination of good ductility and strength. In the case of WCB steel, it has a 36 ksi yield strength, 70 ksi tensile strength and the 22%elongation as minimum tensile requirements. When ductile materials like WCB steel fail, they fail due to the nucleation, growth and coalescence of voids from imperfections in the metal matrix at the grain boundaries. The stages and mechanisms of ductile material failure are shown in Figure 1. Voids nucleate at imperfections in the metal matrix such as inclusions when the inclusion (for example) no longer adheres to the metal matrix. After void nucleation (Figure 1 b), voids grow due to increasing hydrostatic stress and plastic strain (Figure 1c). Due to void nucleation and growth, the void volume fraction is increasing as the strain increases. At some point the voids begin to interact (Figure 1d). The void volume fraction at which interaction between voids begins is called the critical void volume fraction f_c. As the plastic strain continues to increase, local necking occurs in the material connecting the voids until the voids coalesce into a connection of voids and failure occurs. The void fraction at which fracture occurs is the failure void volume fraction f_F . If voids nucleate readily in a material, the overall fracture behavior is determined more by the void growth and coalescence mechanisms, and, conversely, in some materials the void nucleation mechanism controls the fracture behavior and failure occurs rapidly once the voids nucleate [1].

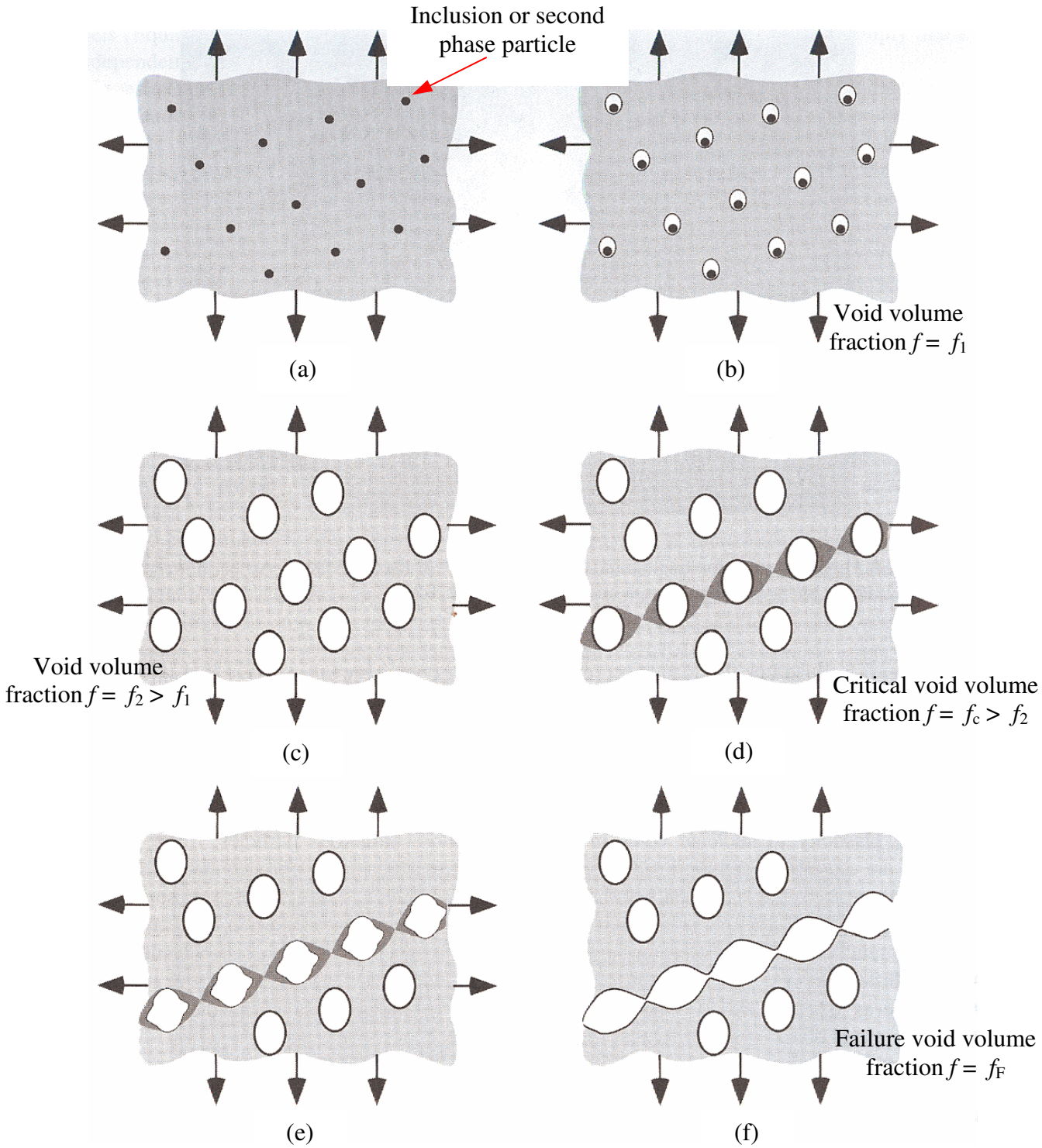

Figure 1 Stages and mechanisms of ductile failure from [1]: (a) imperfections such as inclusions in the ductile matrix, (b) voids nucleate at the imperfections, (c) voids grow and f increases, (d) strain interactions and localization between voids begin at the critical void volume fraction f_c, (e) plastic yielding and necking between voids, and (f) void coalescence and final failure at the failure void volume fraction $f = f_F$.

The preceding discussion relates to the micro-scale of the metal. The effects of porosity on the structural performance of carbon and low alloy steel castings on the macroscopic scale are not that well understood. Reviews of literature were conducted in the areas of stiffness, strength and component life prediction in the presence of porosity and are given in [2,3]. Microporosity may not result in loss of stiffness, localized stress concentration or stress redistribution, but it can greatly affect fatigue resistance [4-7]. Microporosity will affect the ductility of the metal, since the microvoids discussed regarding Figure 1 pre-exist before any stress is applied. Macroporosity in metals (often defined as porosity visible without magnification, typically > 100 μm) can cause gross section loss, locally reducing the effective elastic modulus or stiffness [8-10]. This level of porosity will not be uniformly distributed throughout the entire cast part, and the effective casting material properties are non-homogenous. Stress-strain redistribution occurs in the part due to the pores, and stress concentrations occur near pores, which lead to localized plastic deformation and the development of micro-cracks which lead to failure.

The stiffness and strength behavior of porous materials can be categorized into three classes based on porosity level [11]. These porosity levels are, approximately: 1) less than 10%, 2) 10% to 70%, and 3) materials with greater than 70%. This division is promoted because the materials at the extremes (< 10%, and > 70%) behave quite differently and are described using disparate fundamental assumptions. The extreme high porosity group is not applicable to cast steels; these are foams and cellular structures. Stiffness of materials in the lowest range porosity range can be described by a linear dependence on porosity, derived with the assumption that voids do not interact [12]. Yield and strength behavior in the lowest range of porosity (less than 10%) appears adequately described by considering isolated pores (or voids) [13], or a uniform distribution of pores [14]. These models applying readily to the ductile failure mechanisms illustrated in Figure 1. Perhaps the most used of these micromechanics-based models is the *porous metal plasticity* model describing the plastic behavior and failure of "mildly voided" materials. It is available as a material model in the finite element analysis software *ABAQUS* [13-16]. Using the volume fraction of porosity/voids (or their inverse, the relative density) as the primary state variable, the inelastic flow of the material is modeled as voids grow and coalesce at higher strains until failure occurs. Porous metal plasticity model is used in the work described in this paper to predict the elastic-plastic behavior of cast steel with porosity. The elastic-plastic behavior of the porous materials in the 10% to 70% porosity range has a non-linear dependence on the porosity amount [2,8-10]. A study, described in this paper, was performed to investigate the possibility of merging methods to predict the elastic-plastic behavior of steel with porosity regardless of the porosity level. Ten castings were produced with centerline porosity. The castings were radiographed, and the metal density and porosity level were quantitatively determined from the radiographs. The castings underwent tensile testing. Using the porosity data from the radiographs, finite models of the plates with porosity were developed and the tensile testing was simulated. The results of the simulated tensile behavior of the castings are compared with the measured tensile and failure behavior.

II. PROCEDURES

Method Used to Simulate Elastic-Plastic Response and Failure of Castings with Porosity

Porous metal plasticity was selected as the ductile plasticity and failure material model in this work. The model is based on the work by Gurson [13], who developed a yield condition for a

dilute porous material (approximately < 10% porosity) that is primarily driven by the void volume fraction *f*. In casting simulation, this is typically called the porosity fraction which is the volume of porosity V_{pore} in the sound metal matrix divided by the entire volume of material V_0 (volume of porosity plus volume of sound metal matrix) or

$$f = \frac{V_{pore}}{V_0} \tag{1}$$

In the modeling approach used here, elastic mechanical properties as a function of porosity are used. The elastic behavior is simulated using porosity dependent properties that vary locally with the porosity field in the castings. The following relationship between the elastic modulus and porosity was used locally node-by-node in the FEA analysis [2,17]

$$E(f) = E_0 \left(1 - f/0.5\right)^{2.5} \tag{2}$$

Here for WCB steel E_0 = 198 GPa. The Poisson ratio ν was dependent on porosity *f* using

$$\nu(f) = \nu_S + \frac{f}{f_\infty}\left(\nu_\infty - \nu_S\right) \tag{3}$$

with ν_∞ = 0.14, f_∞ = 0.472 and the Possion ratio for the sound metal was taken as ν_S = 0.3. The elastic model used in *ABAQUS* [16] to model the small strains that occur below the yield stress of the material is

$$\sigma = D_{el}\,\varepsilon_{el} \tag{4}$$

where σ is the total stress, D_{el} is the fourth order elasticity tensor, and ε_{el} is the total elastic strain. Note that Equation (4) reverts to Hooke's Law for the case of uniaxial tension, since D_{el} becomes *E* for uniaxial tension.

Porous metal plasticity in *ABAQUS* requires that a metal plasticity model describe the hardening behavior of the metal matrix without porosity (sound material). Specifically, the plasticity model must give the hardening curve as the yield stress (also called the flow stress) as a function of plastic strain in the sound material. When defining these values the true stress-strain values must be used. In the present study, this data was determined from tensile test data for sound WCB steel shown in Figure 1.

Yield conditions describe the limit of the elastic and onset of the plastic behaviors of materials. The Von Mises yield condition (or criterion), for example, defines yielding as occurring when the Von Mises stress exceeds the yield stress of a material determined in a tensile test. In the porous metal plasticity model used here [16], the yield condition is given by

$$\Phi = \left(\frac{q}{\sigma_y}\right)^2 + 2\,q_1\,f\,\cosh\left(-\frac{3}{2}\frac{q_2\,p}{\sigma_y}\right) - \left(1 + q_3 f^2\right) = 0 \tag{5}$$

where *f* is the porosity or void fraction, *q* is the effective Von Mises Stress, *p* is the hydrostatic stress, σ_y is the yield stress of the fully sound material as a function of plastic strain (used here as shown in Figure 1), and q_1, q_2 and q_3 are material parameters. Note from Equation 5 that when *f* = 0 (for fully sound material), the yield condition becomes $q = \sigma_y$, or the Von Mises yield

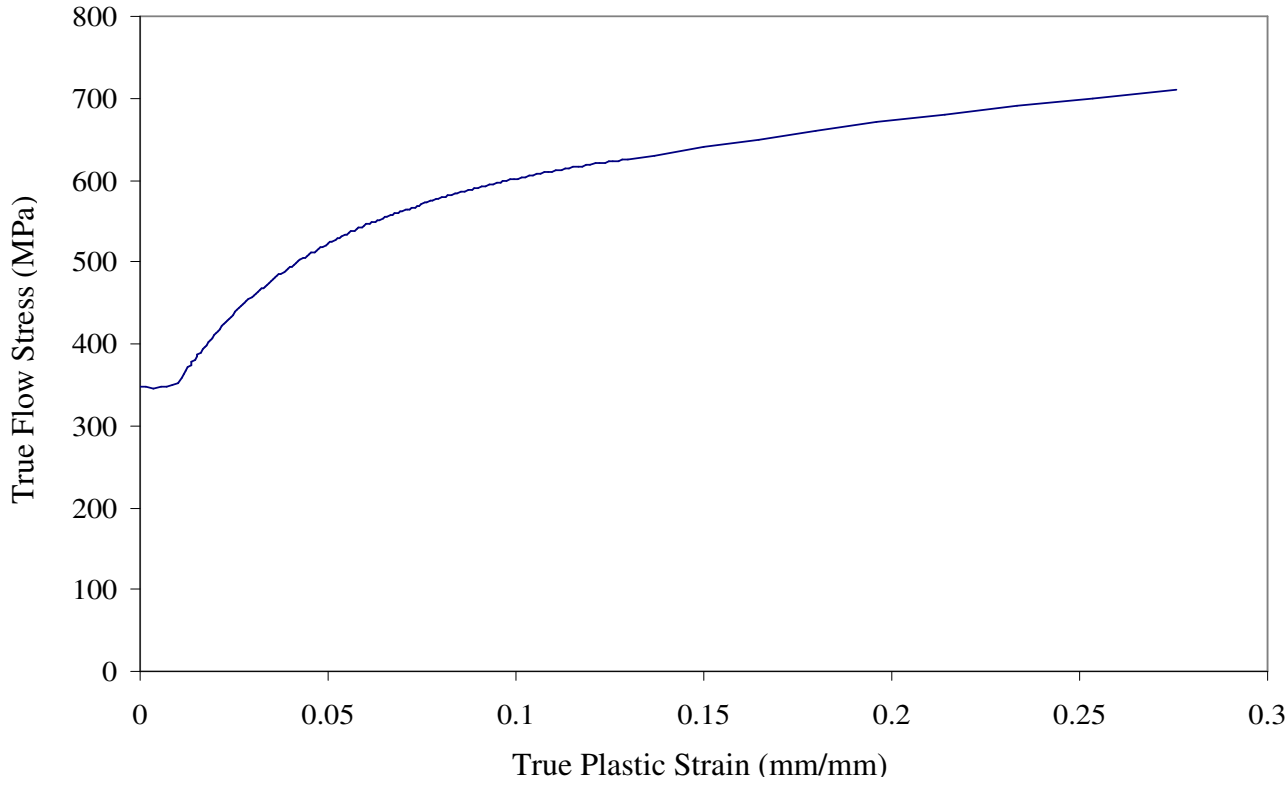

Figure 1 Plastic true stress-strain curve determined from tensile tests of sound WCB steel.

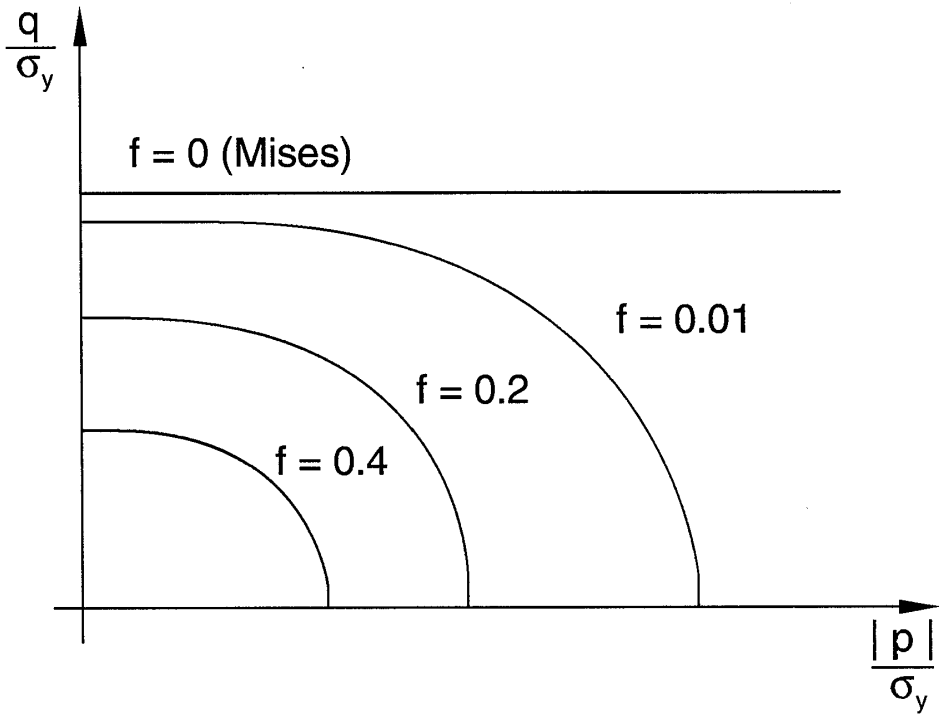

Figure 2 Diagram of yield surfaces from Equation (5) in the *q*-*p* plane for various levels of porosity f = 0, 0.01, 0.2, and 0.4 as taken from [16]. Note that for f = 0 the condition corresponds to the Von Mises Criterion and the surface is not dependent on the hydrostatic pressure *p*.

condition. The yield condition may be visualized as yield surfaces in the *q-p* plane for various levels of porosity *f* (*f* = 0, 0.01, 0.2, 0.4) in Figure 2 as taken from [16] . Note in Figure 2 that for f = 0, the yield condition corresponds to the Von Mises Criterion and also that the surface is not dependent on the hydrostatic pressure *p*.

If σ_1, σ_2, and σ_3 are the principal stresses which can be determined from the multi-axial stress field in *ABAQUS*, the effective Von Mises Stress *q* and the hydrostatic stress *p* are the two stress invariants which are calculated from the principal stresses

$$p = \frac{\sigma_1 + \sigma_2 + \sigma_3}{3} \tag{6}$$

$$q = \sqrt{\frac{1}{2}\left\{(\sigma_1 - \sigma_2)^2 + (\sigma_1 - \sigma_3)^2 + \left(\sigma_2 - \sigma_3\right)^2\right\}} \tag{7}$$

The material parameters in Equation (5) q_1, q_2 and q_3 were added to Gurson's original model [13] by Tvergaard [14] and the original Gurson model corresponds to setting all the material parameters to 1. The material parameters were added by Tvergaard to consider the interactions between voids and improved the Gurson model's accuracy. In the current work we use values for the material parameters that seem to be used often in the literature when applying the model to ductile metals; $q_1 = 1.5$, $q_2 = 1.0$ and $q_3 = 2.25$, where $q_3 = q_1^2$.

The plastic flow is assumed to be normal to the yield surfaces (shown in Figure 2). The yield condition in Equation (5) is used determine the plastic strain to grow voids from the initial void fraction and nucleated voids, and to nucleate additional voids as plastic strain increases. The equation describing the growth rate of voids by growth and nucleation is given by

$$\dot{f} = (1 - f)\,\dot{\varepsilon}_{kk}^{pl} + A\,\dot{\varepsilon}_{m}^{pl} \tag{8}$$

where the first term on the right hand side denotes growth rate from existing voids and the second term denotes the growth rate due to nucleation. The growth rate due to growing existing voids is determined from conservation of mass, and is dependent on the current void fraction *f* and $\dot{\varepsilon}_{kk}^{pl}$, the total plastic strain rate (trace of the strain rate tensor). The growth rate term due to nucleation is calculated by multiplying the equivalent plastic strain rate $\dot{\varepsilon}_{m}^{pl}$ by a scaling coefficient *A*. The scaling coefficient *A* in the *ABAQUS* porous metal plasticity model is

$$A = \frac{f_N}{s_N\sqrt{2\pi}} \exp\left[-\frac{1}{2}\left(\frac{\varepsilon_m^{pl} - \varepsilon_N}{s_N}\right)^2\right] \tag{9}$$

and is based on the assumption that the nucleation function (A/f_N) follows a normal distribution depending on the plastic strain range about a mean value ε_N, a standard deviation s_N and a volume fraction of nucleated voids f_N. Using void nucleation requires fitting the three parameters, and in the current study the values recommended for metals in the *ABAQUS* documentation are used: $\varepsilon_N = 0.3$, $s_N = 0.1$ and $f_N = 0.04$.

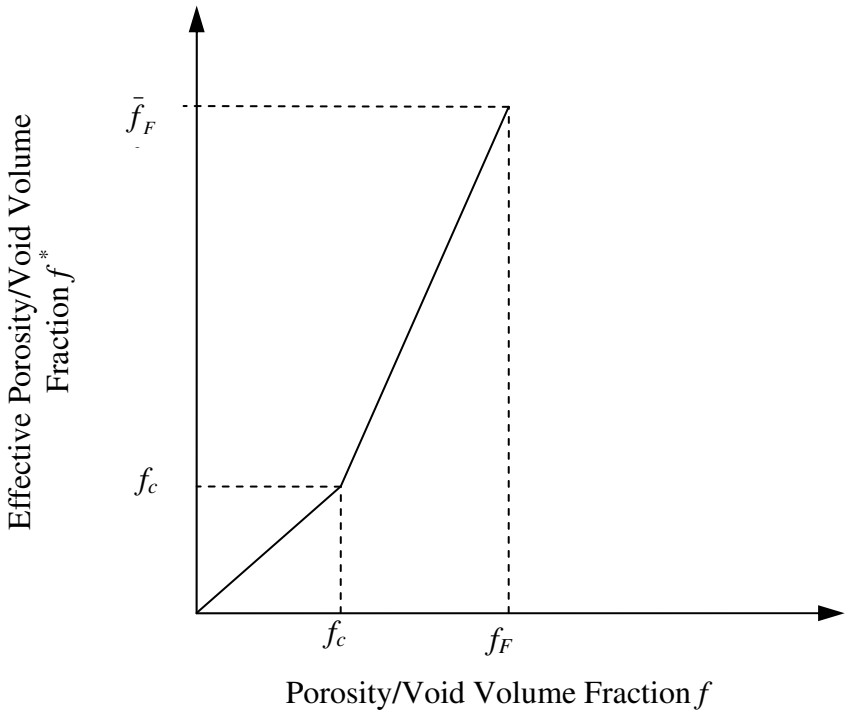

Figure 3 Behavior of the effective void volume fraction in the coalescence model.

A coalescence model and failure criteria model was added to the porous metal plasticity theory by Needleman and Tvergaard [15] where the void fraction f in Equation (5) is replaced by an effective void volume fraction due to coalescence f^*. When f^* is used in Equation 5, it takes on the actual void volume fraction f provided that it is less than some critical value f_c, where coalescence begins. This is shown in Figure 3 for values of $f^* < f_c$, where $f^* = f$. When $f^* > f_c$ the effective void fraction increases more rapidly than f due to the coalescence, which is shown by the steeper sloped region of the plot in Figure 3. Note the slope of this region of the plot, with coalescence, is $(\bar{f}_F - f_c)/(f_F - f_c)$. The material has no load carrying capacity when $f \geq f_F$, where f_F is the void fraction at failure. The equations describing the dependence of f^* on f where f^* is used in place of f in Equation (5) is

$$f^* = \begin{cases} f & \text{if } f \leq f_c \\ f_c + \dfrac{\bar{f}_F - f_c}{f_F - f_c}(f - f_c) & \text{if } f_c < f \leq f_F, \\ \bar{f}_F & \text{if } f \geq f_F, \end{cases} \tag{10}$$

In *ABAQUS*, the value of $\bar{f}_F$ is set using the material parameters by the equation

$$\bar{f}_F = \frac{q_1 + \sqrt{q_1^2 - q_3}}{q_3} \tag{11}$$

In the coalescence model, there are therefore two more parameters that the user should determine: f_c and f_F, the critical and failure void fractions, respectively. In the current work

these values were determined by fitting the model results to measurements for sound WCB steel, and the values used were $f_c = 0.05$ and $f_F = 0.15$.

Procedures for Obtaining Steel Castings with Porosity, Their Radiography and Tensile Measurements

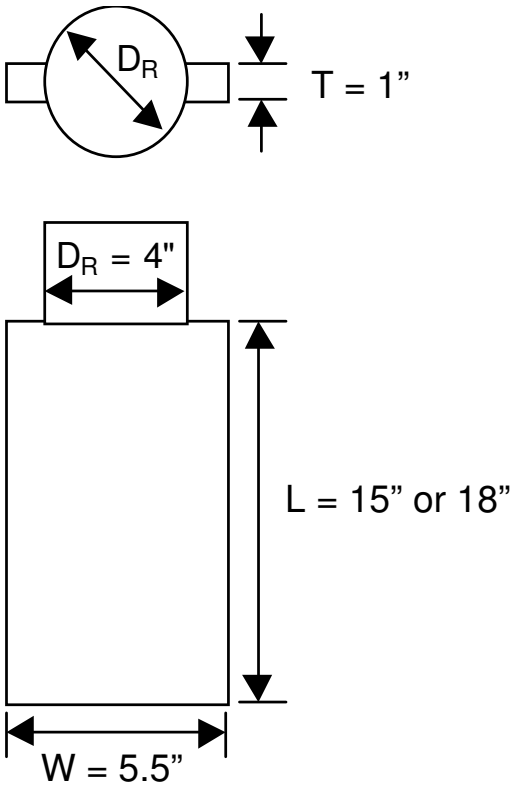

Figure 4 Top and front views of casting geometry vertical plate

In this work, it was important to have a large enough test tensile test specimen to demonstrate the actual performance of a casting with centerline porosity. To obtain cast steel specimens with centerline porosity, 1”T x 5”W x 15”L and 18” L castings were made from ASTM A216 WCB steel. Five castings were produced at each plate length. The as-cast plate geometry is drawn in Figure 4. The castings were produced at an SFSA member foundry and cast vertically as shown in Figure 5, where the 18” long casting is shown in the left side image. The rigging shows a top riser through which it was filled. The castings were designed through simulation to produce centerline porosity as shown in Figure 5 (right side image) for the mid-width slice. The plates were normalized and tempered at Sivyer Steel Casting in Bettendorf, Iowa prior to machining into tensile specimens. From the as-cast plates, 0.75” thick tensile test coupons were machined and their dimensions were determined according to ASTM E8 tensile test standard. The test specimen dimensions are shown in Figure 6. The position of the extensometer is shown in that figure, clipped to the specimen edge. Two small specimens were also machined from the plate castings from an end-effected zone to provide the sound WCB tensile property values for the elastic modulus, yield stress, ultimate strength, and elongation , E_0, σ_{y0}, UTS and EL%.

Radiography was performed on the as-cast plates at the foundry. All the as-cast plates were

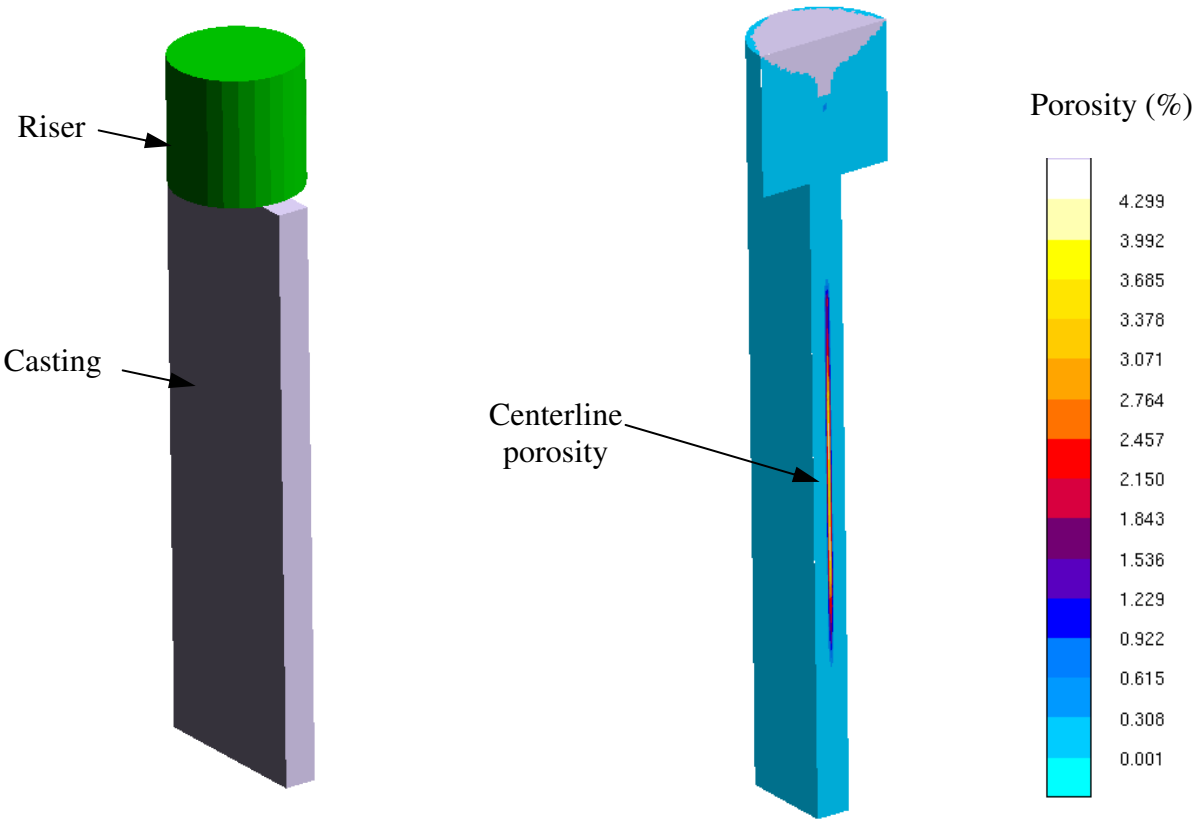

Figure 5 Castings produced with centerline porosity to study its effects on tensile properties.

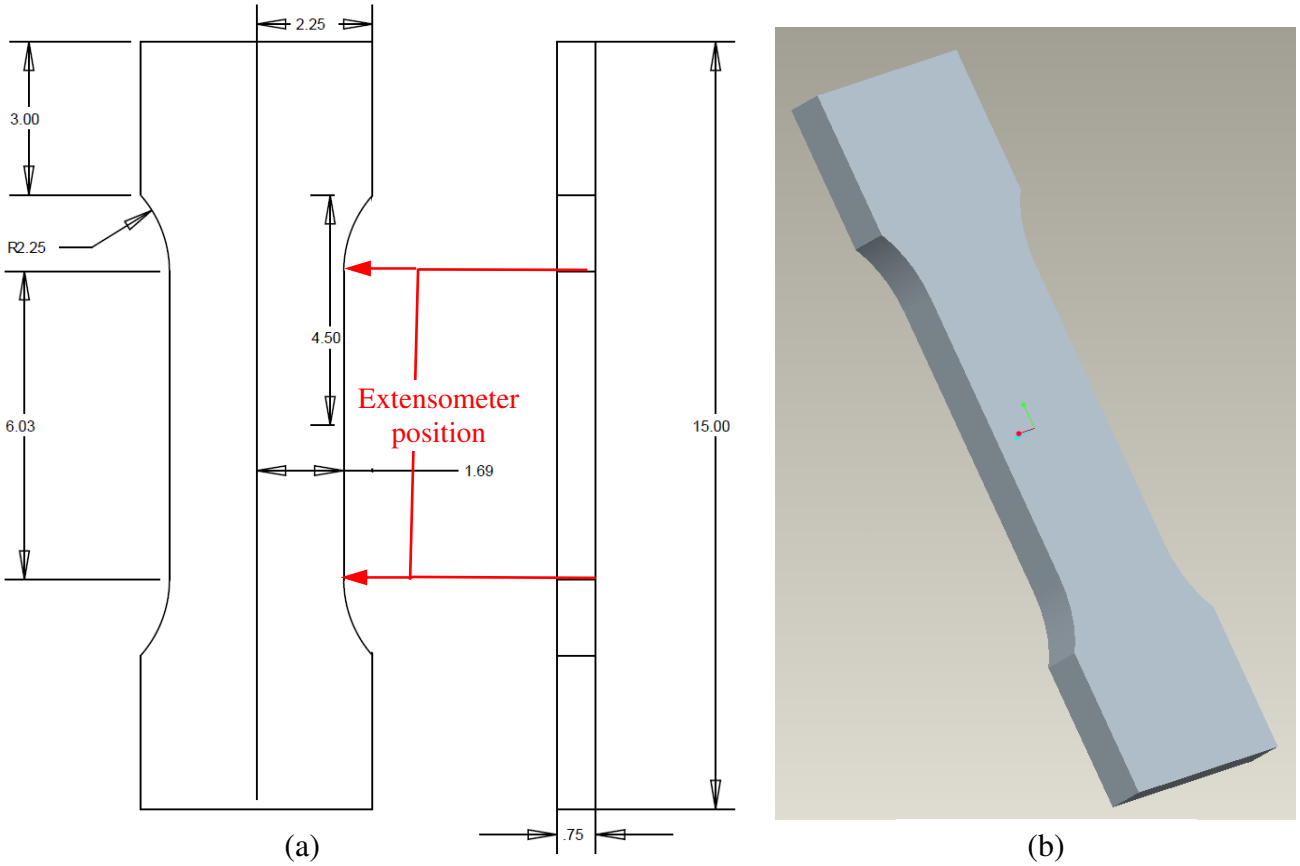

Figure 6 (a) Dimensions (inches) and (b) rendering of machined test coupon used in current study. Position of extensometer is indicated is (a), clipped to edge of specimen.

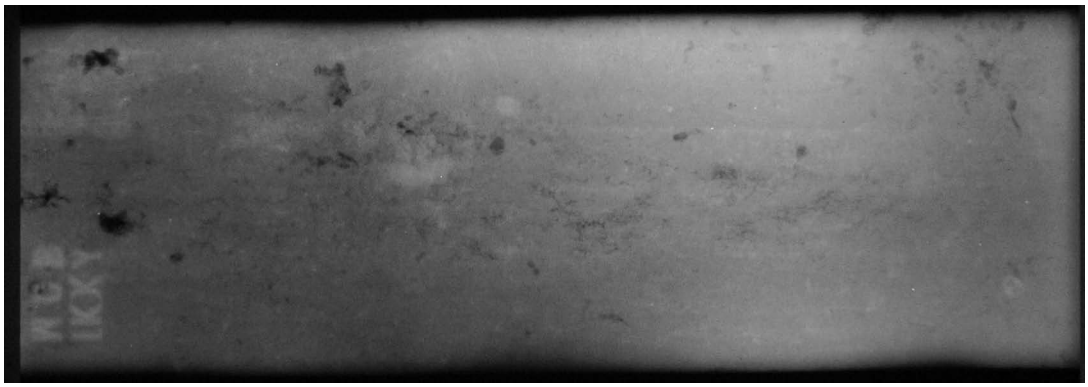

(a)

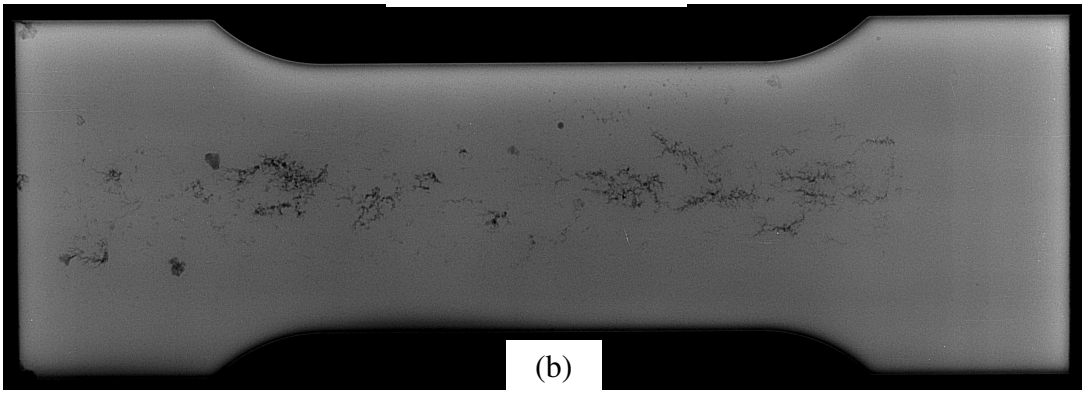

(b)

Figure 7 Radiographs of (a) as-cast plate, and (b) machined 0.75” thick tensile test coupon.

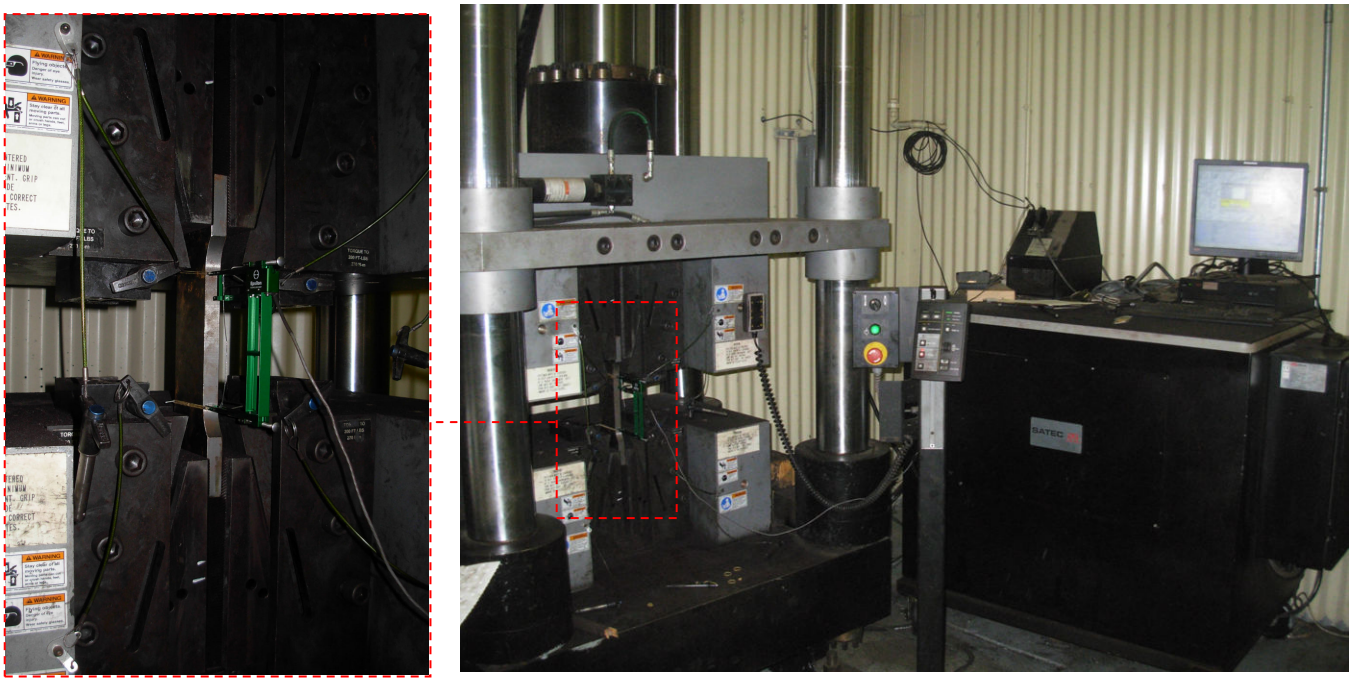

Figure 8 View of test coupon with 6” extensometer fixed to narrow face (image at left) and test machine and controller (image at right).

rated at 4 or 5 severity level by ASTM E446. An example radiograph of an as-cast plate is shown in Figure 7(a). Film and digital radiographs of the small sound specimens and unsound 0.75" thick coupons were made at Alloyweld Inspection, Bensenville, IL, and an example radiograph for the test coupon is shown in Figure 7(b). The test coupon film radiographs were rated according to a new RT standard in the Solidification Laboratory at the University of Iowa by two trained personnel. There was excellent agreement between their measurements of the maximum indication fraction F. The test coupon gage section width was used as the feature length L_f. According to the new RT standard, the tensile plates rated in the fourth and fifth worst acceptance levels out of five [18].

Tensile testing was performed according to ASTM E8; for the sound specimens at University of Iowa, and for the ten 0.75" thick plates at SSAB North American Division, Muscatine, Iowa. It was important to use a large tensile testing machine for the plates with centerline porosity. As shown in Figure 8, an Instron 3500KN (800,000 lb) Tensile Test machine with Instron 5500 Control Unit controlled by Instron Partner Software was used at SSAB to perform the tests. Note in Figure 8 that the 6" extensometer was mounted on the narrow face (thickness edge) of the test coupons because of the configuration of the machine and grips. Photographs were taken of the plates during testing, and the orientation of the plate was recorded, since the deformation of the plate would not be uniform.

Procedures for Measuring Porosity in Steel Castings and Its Use in Simulations

Digital radiographs of the tensile test plates were analyzed to determine the porosity in the plate section from gray level density measurements. Stepped blocks of known thickness and a 0.75" thick penatrameter were placed in each radiograph. From the gray level density values on the radiographs at these, a calibration was established between gray level and steel thickness for each radiograph. For example, in Figure 9(a) a digital radiograph of a tensile test plate is shown. Note the stepped gage blocks on left side of that image, and that the steps are selected using a yellow rectangular tool that averages gray level across its width. There is a "Start" and "End" point indicated along the selection tool length. In Figure 9(b) the measured average gray level along the steps is plotted from the start of the rectangular tool until the end. For the stepped blocks that are thicker that the plate (0.75") the data is not used. Gray level increases as the step block thickness decreases, and sensitivity is lost at the block 0.31" thick. From the 0.75" to the 0.31" thick blocks, there are eight blocks that can be used to determine a thickness versus gray level calibration curve for the gray level density indications on the radiograph. This calibration curve for one of the radiographs is shown in Figure 10, and after evaluating each radiograph in this way, all curves were found to fall within the gray level uncertainty bars in Figure 10. In addition, a method was devised to filter out shadows on the radiograph and determine what is or is not an indication. Only pixels identified as indications were analyzed to determine the plate thickness, otherwise the plate at a given pixel was considered to be sound. This process is demonstrated in Figure 11, where from left to right is shown an original radiograph image, image of indications detected by analysis (black pixels for indications, white for sound), and the thickness of tensile test plate measured from image analysis and calibration curve. Finally, the thickness at a pixel, as shown in Figure 11, is divided by the plate thickness (0.75") to determine the porosity at a given pixel location on the radiograph as shown in Figure 12.

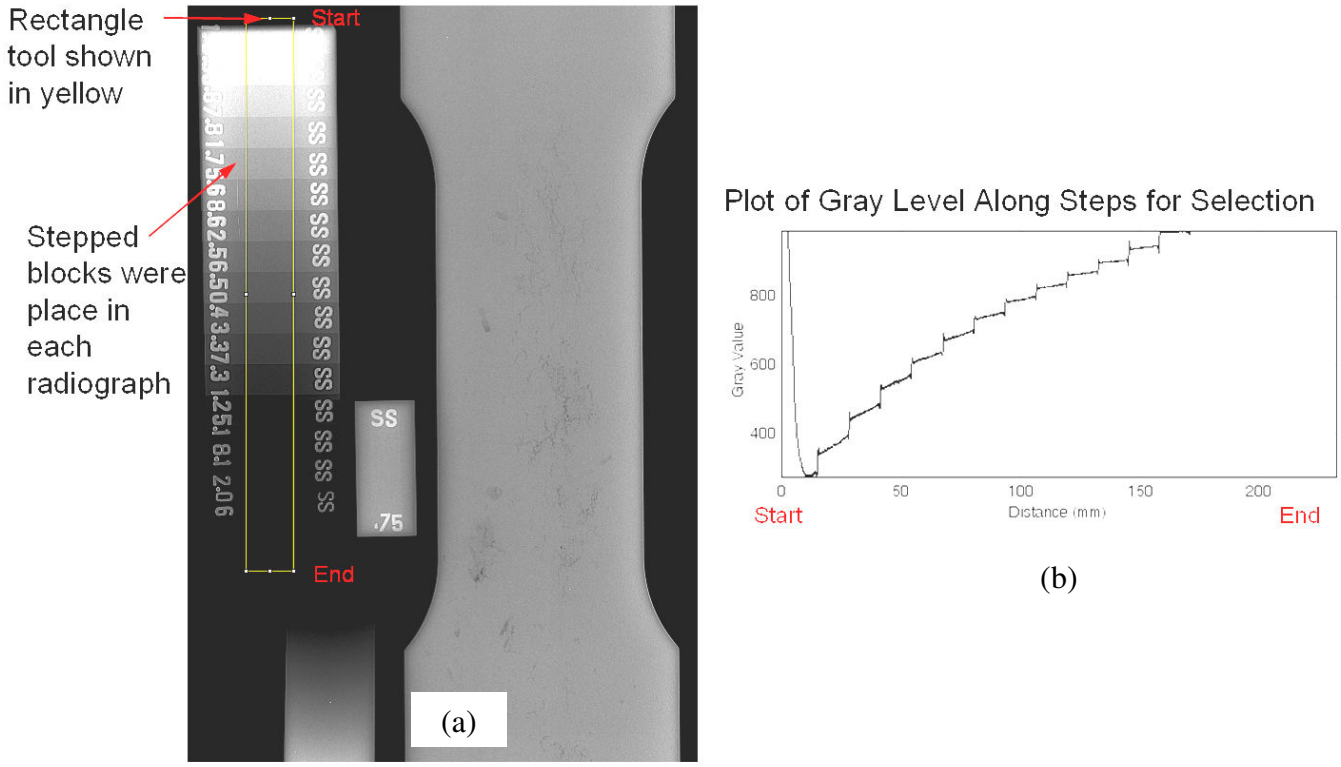

Figure 9 (a) Digital radiograph tensile test plate showing stepped gage blocks on left side of image. The steps are selected using a rectangular tool that averages across its width. (b) The gray level along the steps is plotted from the start of the rectangular tool until the end.

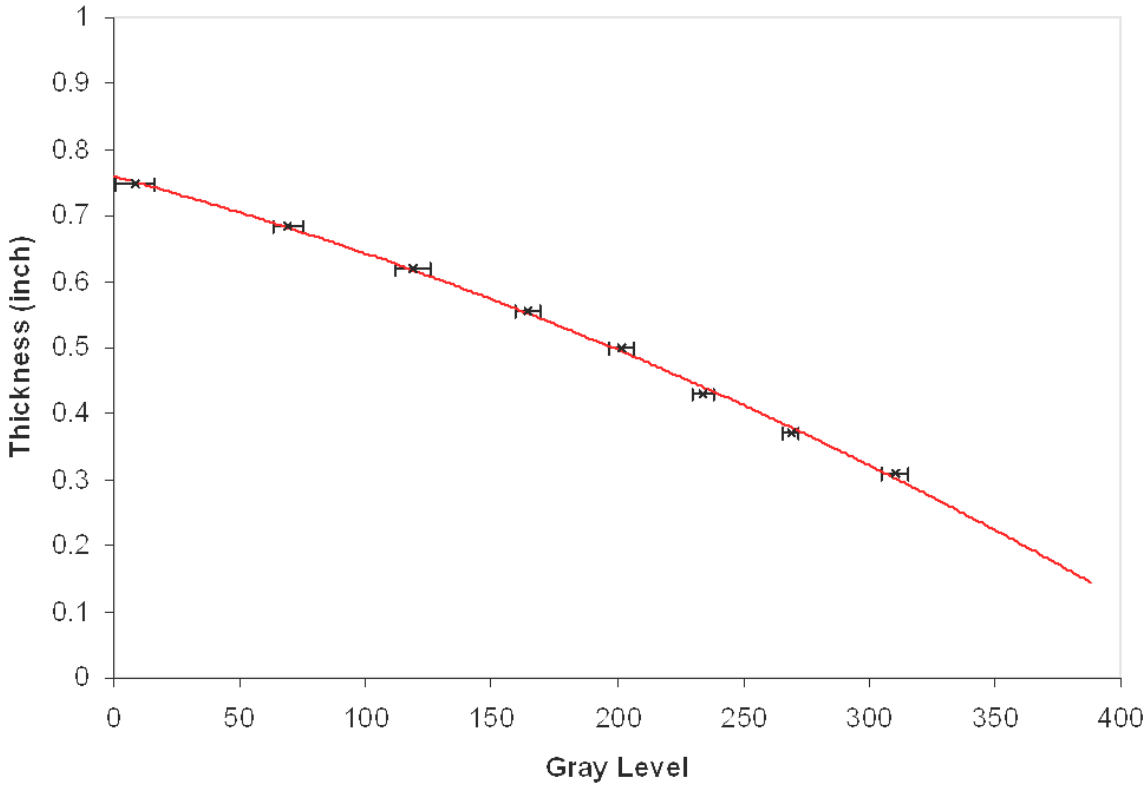

Figure 10 Example thickness versus gray level plot developed from data from the stepped blocks.

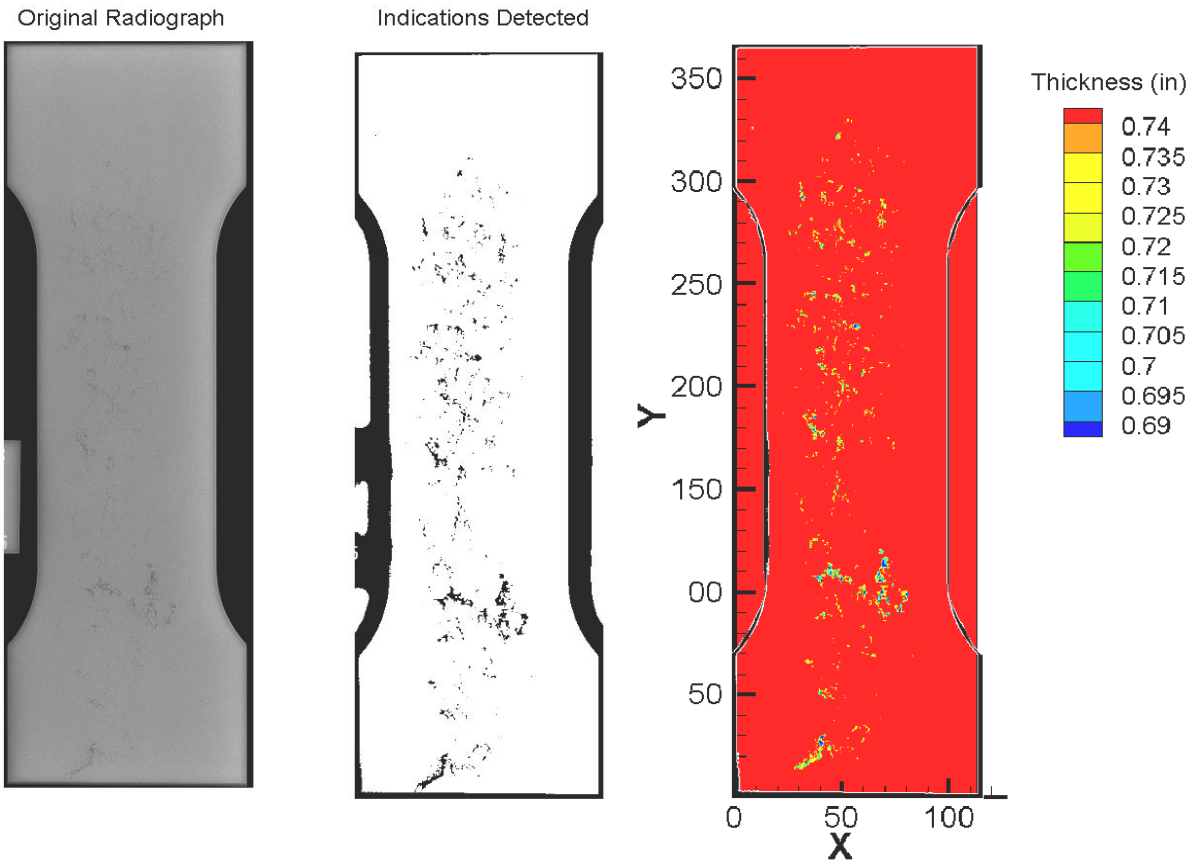

Figure 11 From left to right, original radiograph image, image of indications detected by analysis, and thickness of specimen measured from analysis.

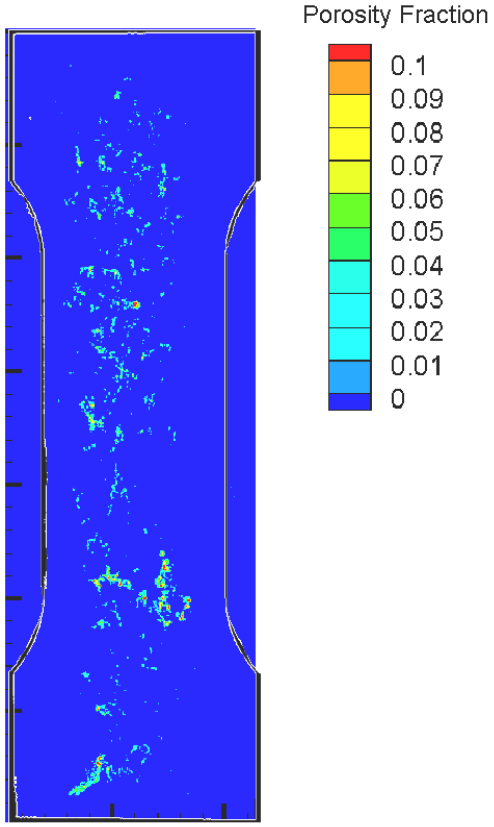

Figure 12 Example of porosity measurement through the section thickness of a tensile plate.

After determining the through section porosity in the tensile test plates from the radiographs, the porosity was transferred to the finite element model for use in simulating the testing. The difficulty at this point was that only the porosity for the entire through section of the plate was known, and it is clear that the porosity is not this uniform value through the plate thickness. At the other extreme limit, it is not true that the porosity corresponds everywhere to a complete hole, a hole that would have a through plate dimension equal to the sound minus measured plate thicknesses. In order to determine how the porosity is distributed through the plate thickness,

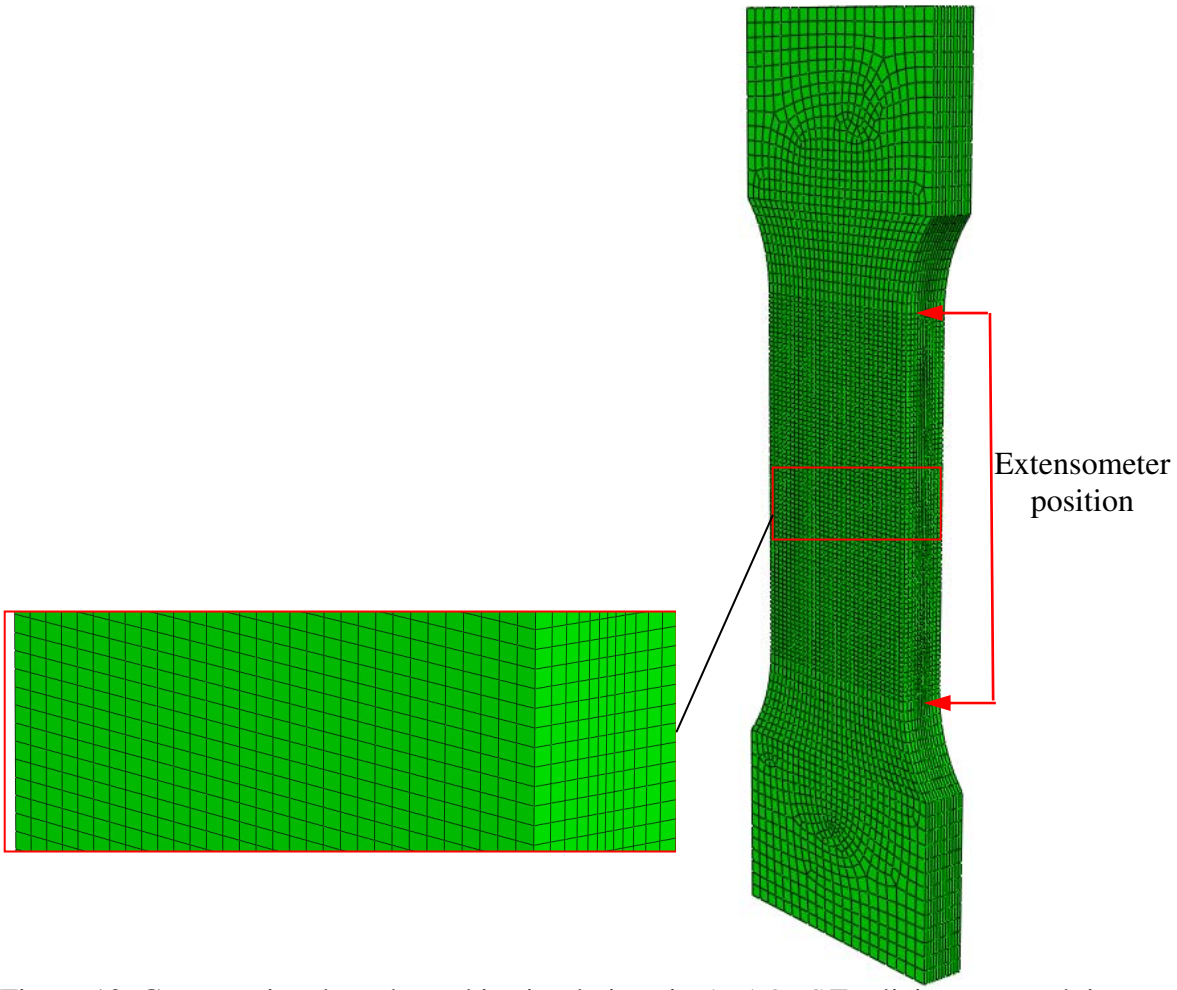

Figure 13 Computational mesh used in simulations in *ABAQUS* Explicit, note mesh is slightly biased toward finer spacing near the mid-thickness.

additional radiographic views and x-ray tomography is required. Acquiring such data was beyond the scope of the current project, since here the goal was to use radiographic data such as that available to a foundry in the analysis. Numerous simulation studies were performed to arrive at a reasonable assumption for how the porosity is distributed in the plate thickness. Some of these studies were performed to determine the best finite element mesh that could be used for the simulations, on which the porosity in the plates would be mapped. The mesh that gave the best compromise between simulation time and accuracy is shown in Figure 13. Note that the mesh was developed to have finer spacing in the test plate gage section, and finer spacing toward

the mid-thickness of the plate. In addition, the interpolation method used to map the porosity from the radiographic data to the mesh node point was developed to calculate average porosity about the mesh node spacing from the radiographic data. This way the porosity from the radiograph is conserved when mapped to the finite element analysis (FEA) mesh. Based on the typical maximum thickness of material lost due to porosity in the radiographs, it was decided to

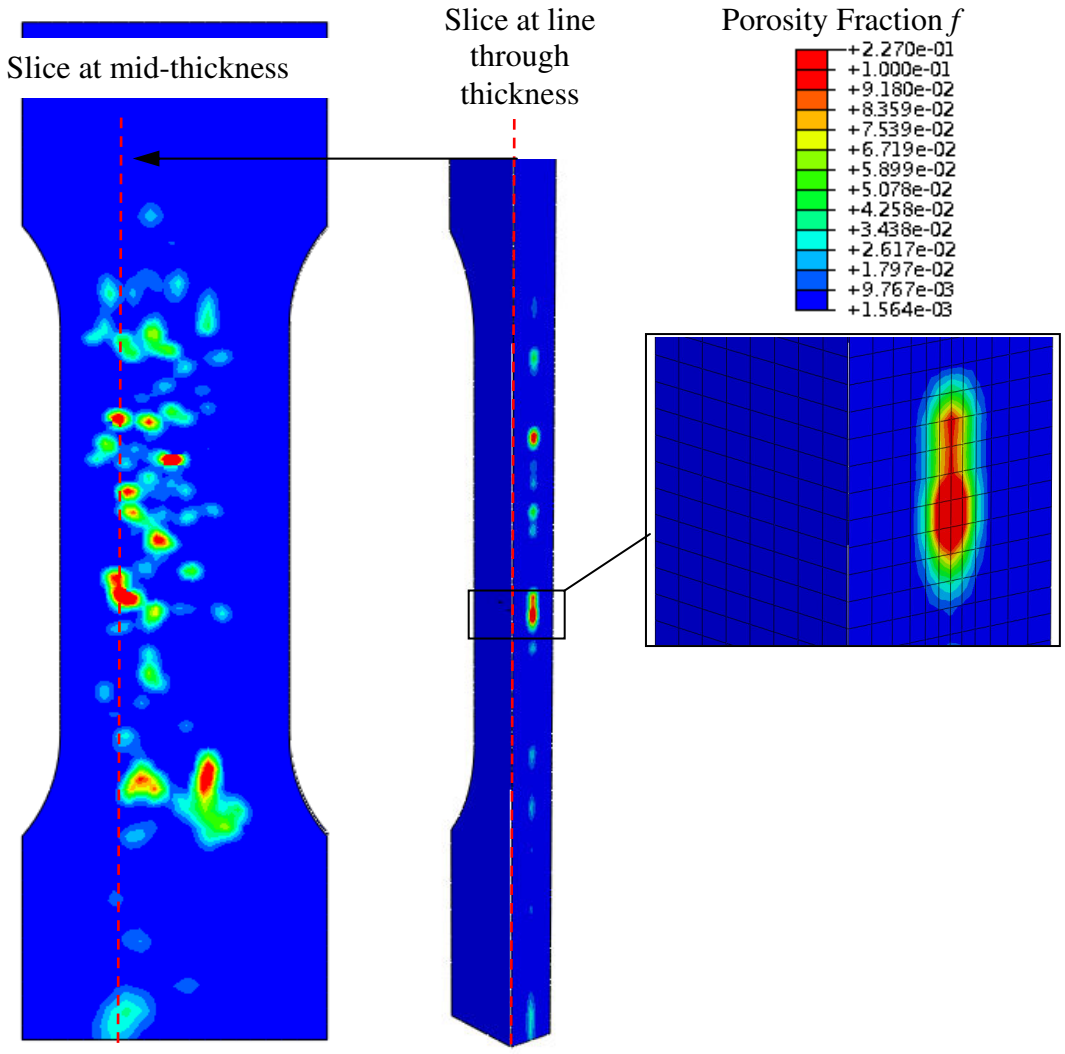

Figure 14 Example of mapping the porosity faction to the mid-thickness plane of the FEA mesh.

distribute the porosity at the mid thickness of the plate in a thickness region approximately 2.2 mm thick at the mid-thickness plane, corresponding to the two centermost elements, one on each side of the plate mid-thickness. All nodes in these elements are set to the porosity fraction determined by multiplying the through section porosity value by the entire plate thickness, and then dividing by the thickness of the region (2.2 mm). The highest value of porosity fraction found in all plates when mapped to the centerline by this method was about 57%. An example of the mapping process for the porosity field from Figure 12 onto the finite element model is shown in Figure 14 at the plate mid-thickness plane, and at a plane through the plate thickness as indicated by the dashed red line. Note that *ABAQUS* only allows for the porosity fraction to be

mapped to the finite element nodes, and nodes are shared between elements, so when one examines the porosity field in the post processor as shown in the zoomed image at the right hand side it appear to diffuse outside of the two centermost elements.

Once the porosity is mapped to the FEA model for the ten plates tested, boundary conditions were setup to match the testing conditions. The simulations were run using *ABAQUS* Explicit using a displacement boundary condition at the upper grip end of the plate using a multi-point constraint. The force was determine from the reaction force at the node where the displacement boundary condition was applied, and was confirmed for several simulations by calculating the average stress on the upper face of the plate and dividing by its area. The stress for the simulated tests was determined by dividing the force by the gage section nominal area, just as in the tensile testing. The strain in the simulated tests was determined by the relative displacements of node sets defined at the locations of the attachment points of the extensometer.

III. RESULTS

Results of Tensile Testing

The measured stress-strain test curves for the sound specimen and the ten plates with porosity are shown in Figures 15 and 16. In Figure 15 the full tensile test curves are given, and in Figure 16 the curves up to 0.04 strain are shown to focus on the elastic range and yield points. The sound specimen test data was found to agree well with the standard ASTM A216 WCB properties: elastic modulus E_0 is 27,968 ksi (193 GPa), yield strength σ_{y0} is 52.4 ksi (361 MPa), ultimate tensile strength 80.6 ksi (556 MPa), and the elongation at fracture is 22%. The property values for the ten plates with porosity and the sound data are given in Table 1. Note that in the testing of specimen D1, the UTS and percent elongation were not acquired due to the machine automatically shutting down from an incorrect controller setting. The stopping point of the stress-strain curve for D1 is indicated in Figure 16.

Looking at the elastic modulus results from the testing, note that in Figure 16 the elastic part of the curve is more linear for the sound material than for any of the castings with porosity. This nonlinearity in the plates with porosity is believed to be caused by local yielding and regions within the plate bearing the stress non-uniformly. It was more difficult to determine the elastic modulus for the material with porosity because of the nonlinearity. Because of this, the elastic modulus for the porosity data was determined using a chord modulus between the stress-strain data at 10% and 90% of the yield stress [19]. The stiffness of the plates with porosity is reduced from the sound data in each plate tested. Note that four of the five highest measured elastic modulus plates are from the “D” family of plates, which might not be surprising since the “D” plates have a shorter feeding distance.

In Figure 16 note that the yield strength of the sound material is somewhat below the average of the test plates with porosity. Also note that the “D” specimen plates appear to have generally higher yield strengths than the “E” plates. Just as with stiffness, if one were to rank the test plates by yield strength, four of the five highest measured yield stress plates are from the “D” family of plates that had a shorter feeding distance. The yield stresses of all plates with porosity range from 48 to 56 ksi, and all would meet the minimum yield stress requirement for WCB steel (36 ksi).

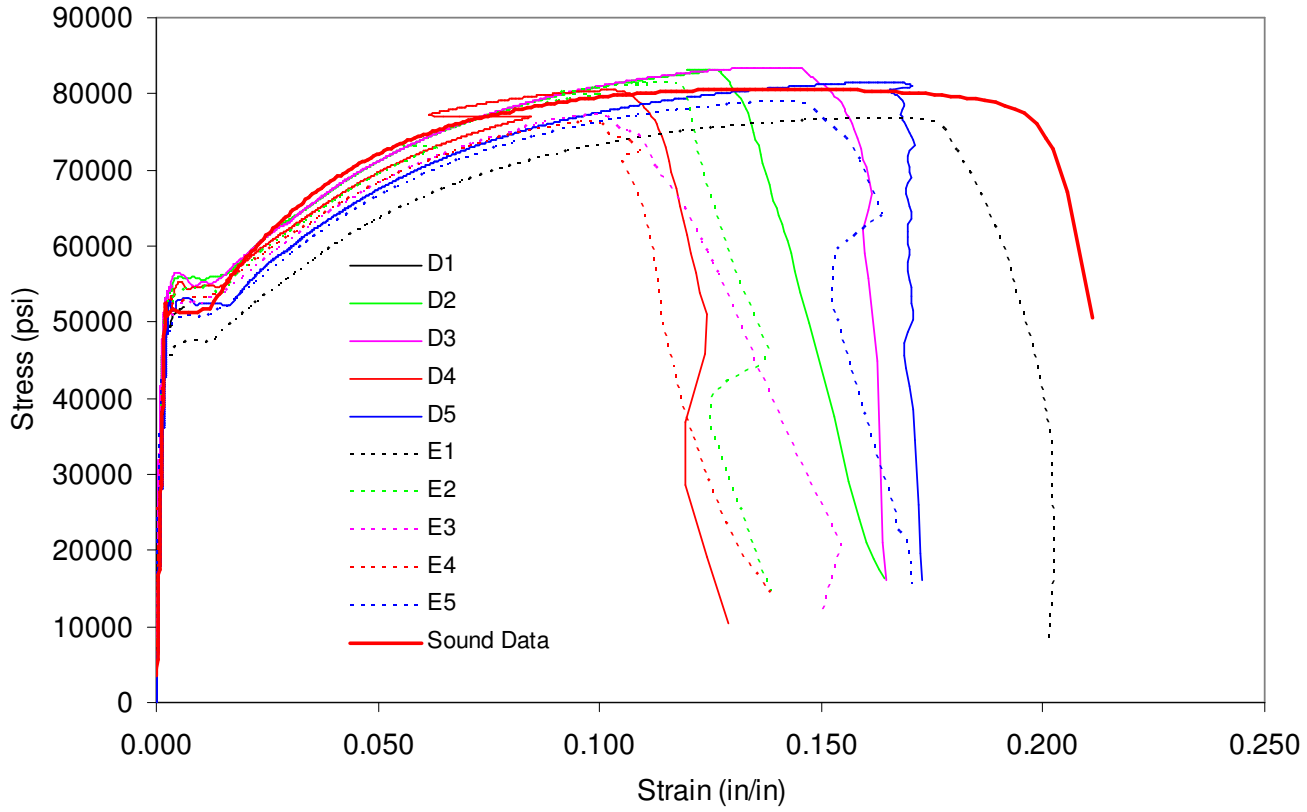

Figure 15 Full tensile test stress-strain curves for sound material and the ten plates with centerline porosity.

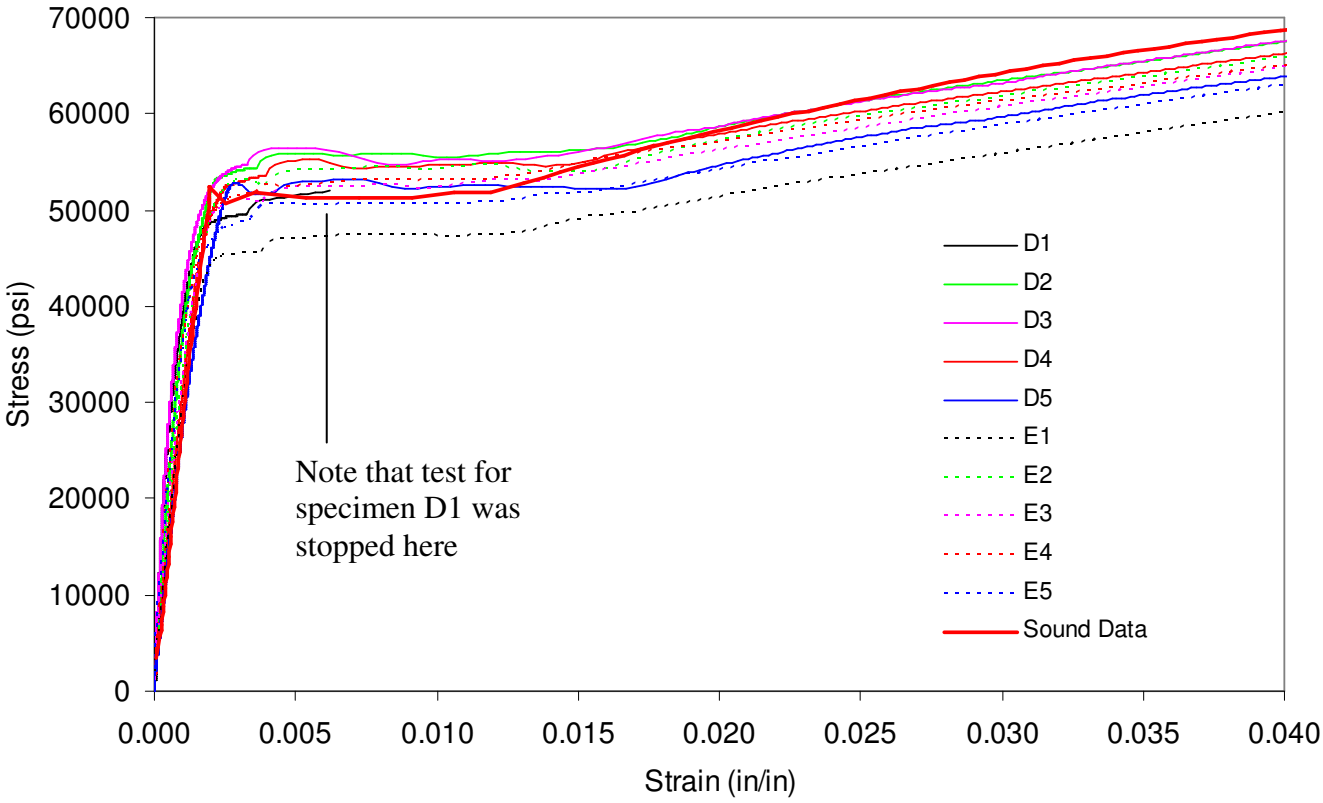

Figure 16 Stress-strain curves showing yield and plastic portions up to 0.04 strain.

Table 1 Tensile property measurements for ten plates with porosity and sound data.

Plate ID	Elastic Modulus (ksi)	Yield Stress 0.2% (ksi)	UTS (ksi)	Elongation (%)
D1	26096	51.01	NA	NA
D2	25109	55.65	83.05	16.00
D3	26055	56.35	83.49	16.30
D4	25260	54.39	80.41	12.80
D5	19907	54.15	83.51	17.10
E1	22796	47.75	78.61	19.60
E2	23586	53.38	81.52	13.80
E3	24971	51.53	77.17	15.00
E4	25927	52.52	76.24	13.80
E5	24518	50.65	78.88	17.00
Sound Data	27600	51.76	80.65	22.00

In Figures 15 and Table 1, the ultimate strength of the sound material is among the highest values measured (80.7 ksi), but not the highest. The range of all UTS data is from 76.2 to 83.5 ksi, and all data meet the minimum UTS tensile requirement for WCB steel (70 to 95 ksi). Again, as with stiffness and yield strength, ranking the test plates by UTS one sees that four of the five highest measured UTS plates are from the "D" family of plates.

The sound material clearly has the greatest ductility with 22% elongation to failure (EL%) as shown in Figure 15 and Table 1. Examining the stress-strain curves from Figures 15, one sees that the plates with porosity have EL% values from 13% to nearly 20%, but the plate with 20% elongation might be an outlier. The reduction in ductility observed in the plates with porosity is perhaps the most obvious effect of the porosity on the tensile properties as seen in Figure 15.

Results of Simulated Tensile Testing

Numerous simulations of the tensile tests for the sound material were run, comparing results to the measured sound data until the "best fit" parameters were determined for use in the *ABAQUS* porous metal plasticity model . Guidance was taken from the literature on the range of values applicable to ductile steels, but it was a trial and error procedure. One parameter used in the model has not been mentioned yet; it is the initial void fraction assumed in the material. Relying on nucleation alone in the model will not give realistic results. A typical value used to simulate ductile failure in steels is 0.2% so that was used. All the parameters used in the model are given in Table 2, and the comparison between the measured and predicted tensile curves for sound material are shown in Figures 17 and 18. The comparison between simulated and measured is excellent. Slight improvement might be gained, but it was determined the additional trial and error effort was not warranted.

Table 2 Parameters used in the porous metal plasticity model for WCB steel in *ABAQUS* simulations.

q_1	q_2	q_3	f_0	f_c	f_F	ε_N	s_N	f_N
1.5	1	2.25	0.002	0.05	0.15	0.3	0.1	0.04

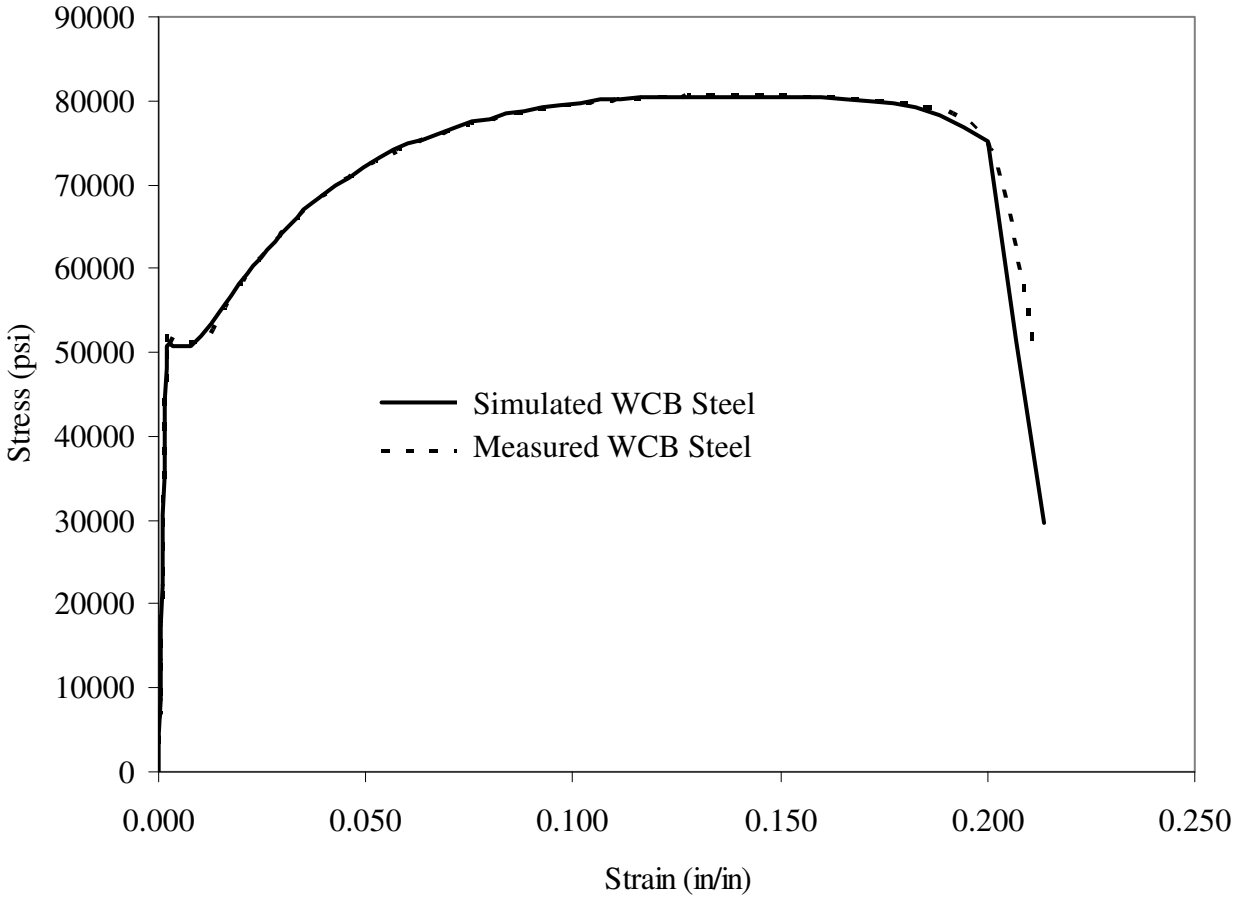

Figure 17 Measured stress-strain curve for sound cast material compared to predicted curve using *ABAQUS* with porous metal plasticity model.

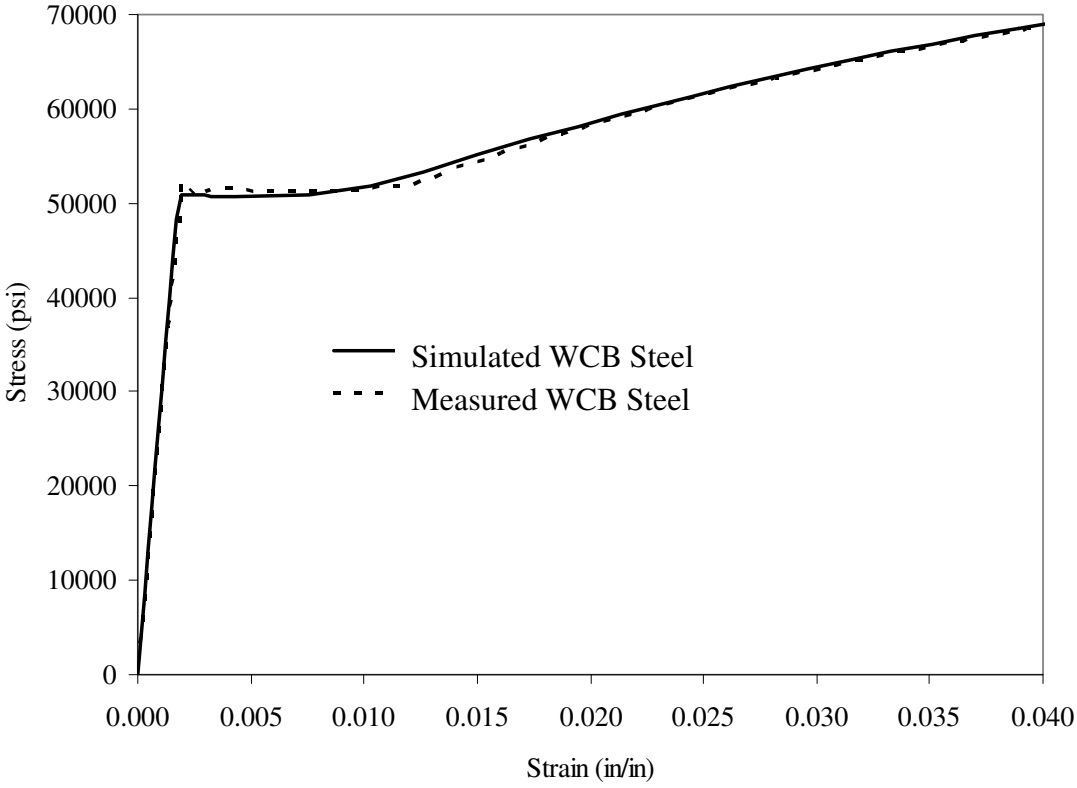

Figure 18 Measured stress-strain curve for sound cast material compared to predicted curve using *ABAQUS* with porous metal plasticity model showing detail at yield point.

As mentioned, there was an operator error running the tensile test of plate D1, and only nine tensile curves for the plates with porosity were simulated. The measured and simulated stress-strain curves for those nine plates are given in Figures 19 to 27. In each figure the measured sound curve is provided as a basis for comparison. The elastic portions of the curves are not shown in detail because there was no observable difference from the sound curves except slightly lower yield stress. The nonlinearity observed in the test data for the plates with porosity was not observed in the simulated plates with porosity. The porosity level at the centerline was too low to affect stiffness. Some of the simulated tensile tests show excellent (i.e. E4) or reasonable (i.e. D4, D5, E2, E3) agreement compared with the measured curve. The elongation to failure, which is somewhat open to interpretation in the simulation results, agrees well overall. One of the most interesting observations is the poor agreement between the predicted and measured curves for specimen E1, which had a markedly lower yield stress and UTS than simulated. On the whole, the simulations generally correctly predict the loss in ductility for the plates with porosity.

The measured and simulated plastic properties (yield stress, UTS and EL%) are summarized for comparison in Table 3. There is variability in the measured yield stress that is not captured by the simulations. The simulations more closely track the sound plastic stress-stain curve (Figure2) than do the measurements. This might be due to placing the porosity at the centerline, or the size of the porous region, or the fact that the radiography (or methods used to analyze it) are not detecting and including all the porosity in the plates. Also, note that none of the simulation yield stresses or UTSs are greater than the sound data. It was hoped to demonstrate that the model might predict the local stress redistribution and hardening that might be responsible for the variability observed in the measured curves (and increased yield stress and UTS compared to sound material). Additional simulation "experiments" need to be performed to see if predicting such behavior is possible with the model. As the model stands, if the plate has any level of uniform porosity, it will never predict a yield stress or UTS greater than that of the sound material. The data in Table 3 are plotted in Figures 28 to 30, where the measured and simulated plastic properties are compared for yield stress, UTS and EL%, respectively. In each figure the line of perfect correspondence is shown and the sound data circled. Clearly in Figure 28, the model fails to predict the variability in the yield stress, and the model conservatively under predicts the yield stress for all castings except plate E1 (indicated in figure). In Figure 29, the model again is conservative in under predicting the UTS. For UTS though it predicts more variability, and more of the trend in the measured data. Finally for EL% in Figure 30, the model generally under predicts the elongation, but the correspondence between the measured and predicted data is much stronger than the data in Figures 28 and 29.

In Figures 31 to 35 the radiographs used to determine porosity, a photograph of the plate after testing, and the simulation results for the Von Mises stress on the plate surface at failure are given for plates D2, D3, D5, E4 and E5, respectively. On the radiographs the maximum indication on the radiograph from the new RT standard is given by the position of the yellow line, and the position of the fracture (which can also be gathered from the photo taken after testing) is indicated on the radiograph by a red line. The location of the failure can only be predicted by exact knowledge and modeling of the actual porosity distribution inside the plate, as distributed throughout the thickness. It is not surprising that locations of the maximum RT indication and failure do always coincide. The porosity distribution in the plates is dependent on the density of indications, and that is not taken into account in the RT standard. Note that the photos of the plates after testing show substantial damage at locations other than the final failure.

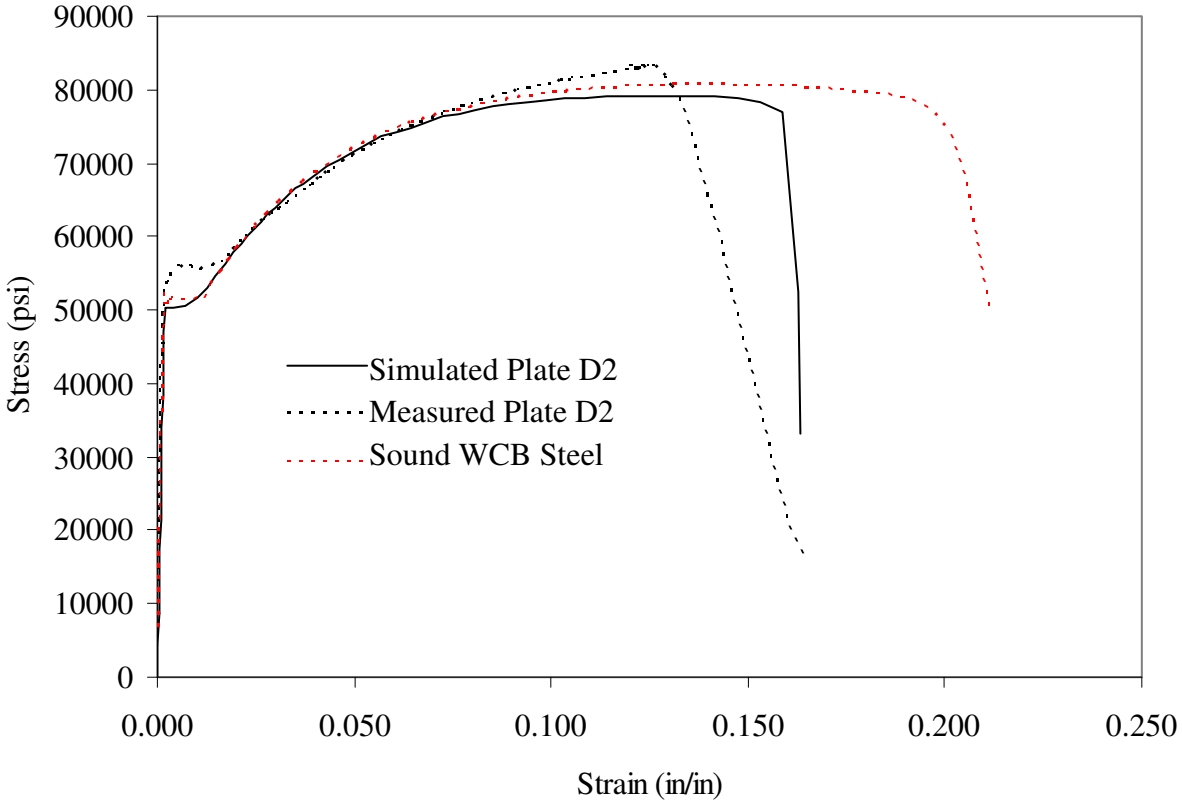

Figure 19 Measured stress-strain curves for sound cast material and plate D2 with porosity are compared to predicted curve for plate D2 using *ABAQUS* with porous metal plasticity model.

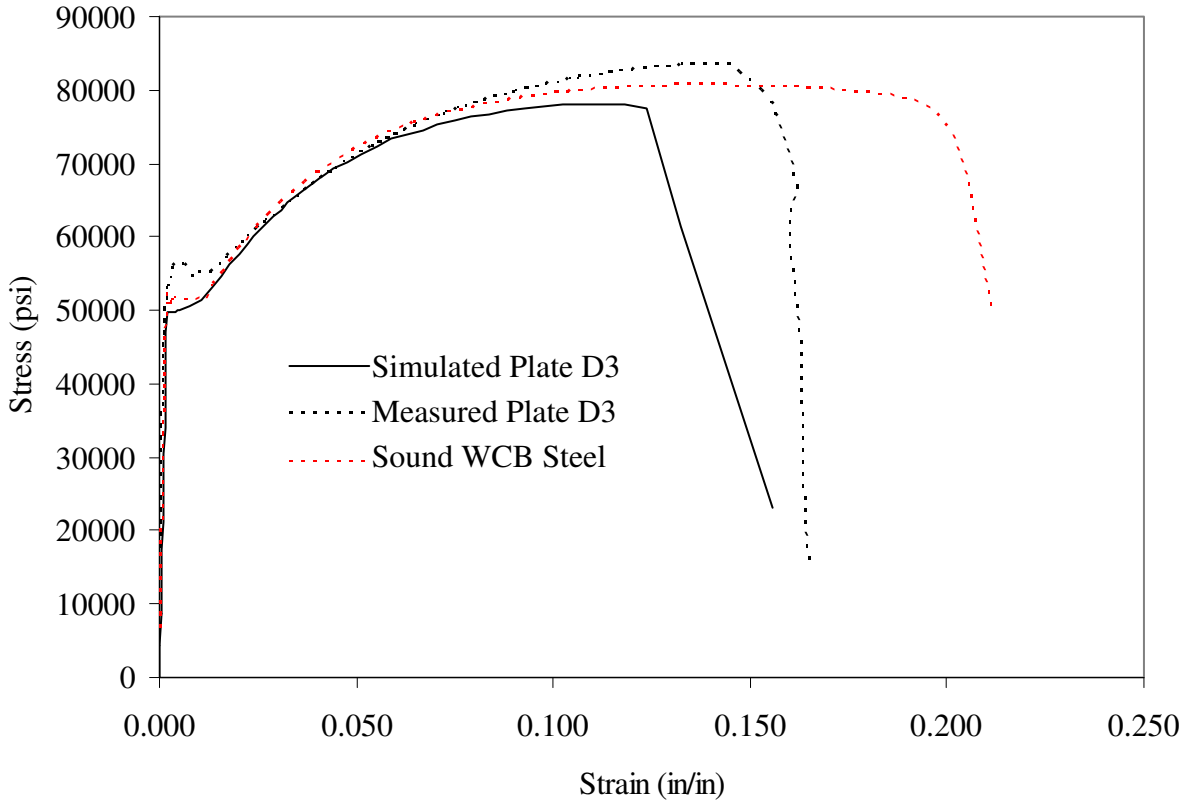

Figure 20 Measured stress-strain curves for sound cast material and plate D3 with porosity are compared to predicted curve for plate D3 using *ABAQUS* with porous metal plasticity model.

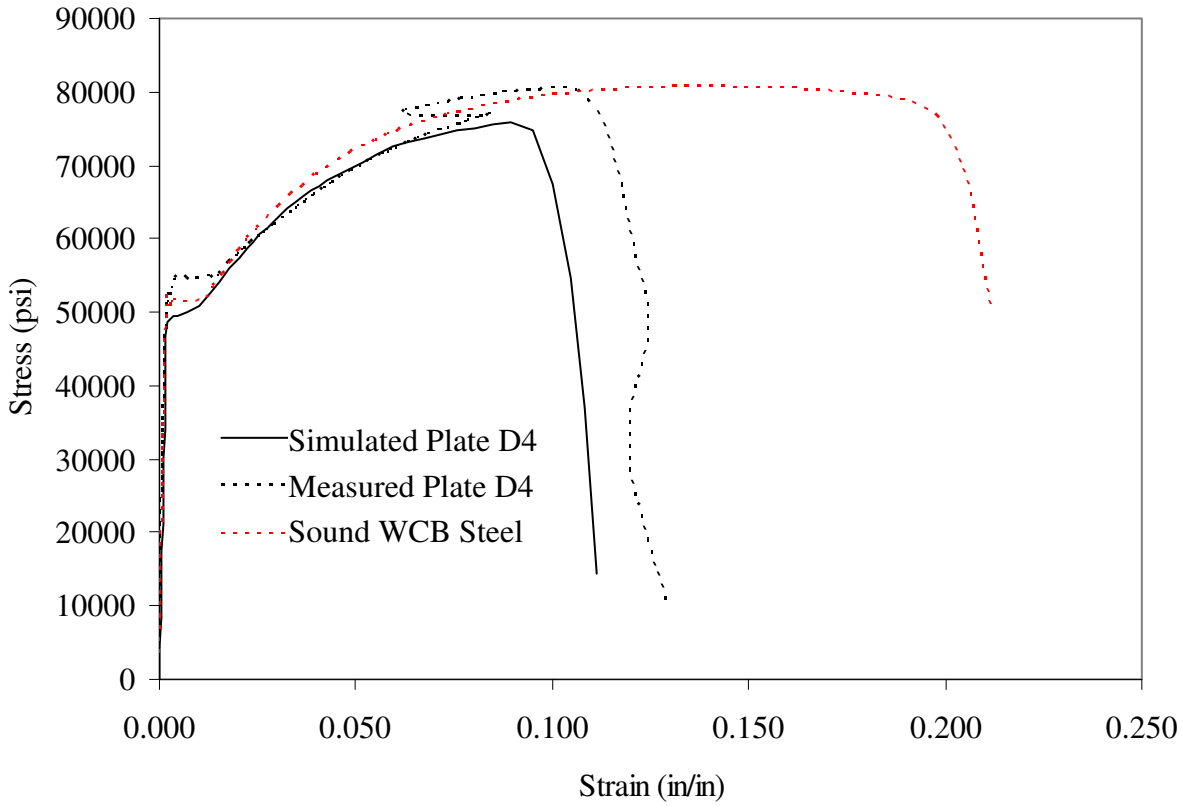

Figure 21 Measured stress-strain curves for sound cast material and plate D4 with porosity are compared to predicted curve for plate D4 using *ABAQUS* with porous metal plasticity model.

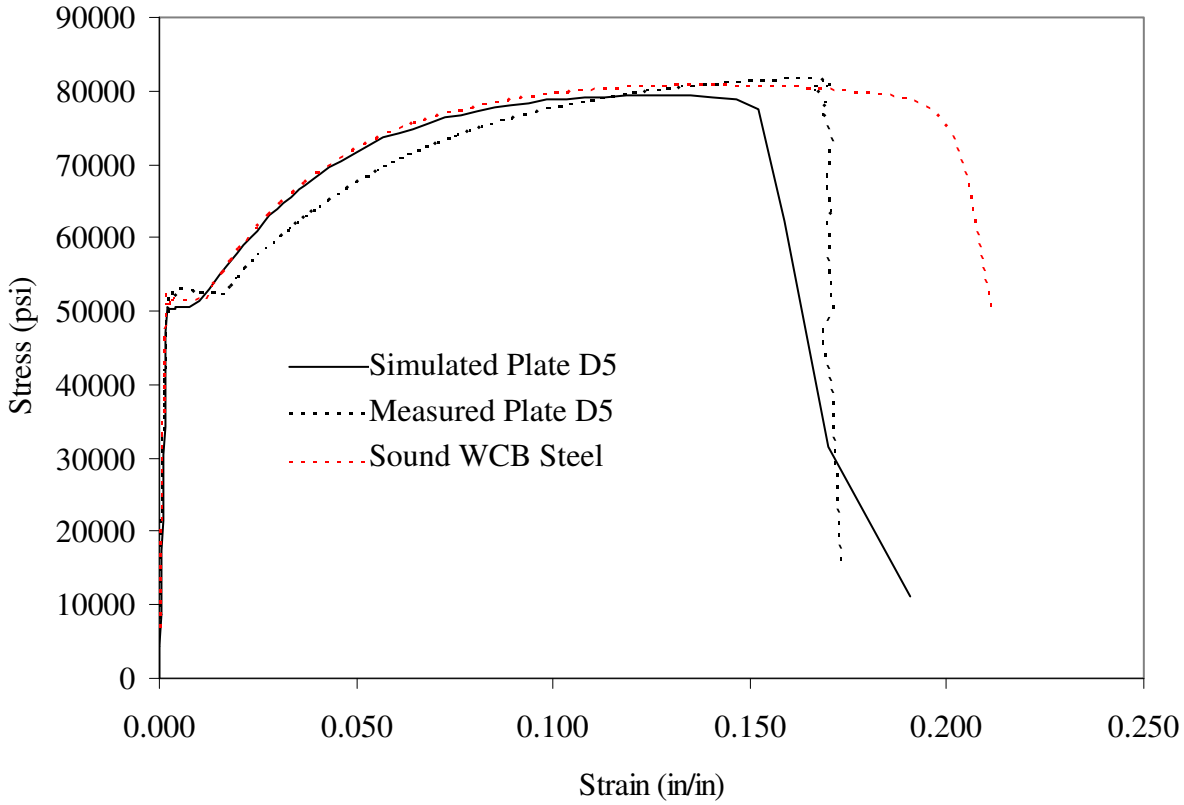

Figure 22 Measured stress-strain curves for sound cast material and plate D5 with porosity are compared to predicted curve for plate D5 using *ABAQUS* with porous metal plasticity model.

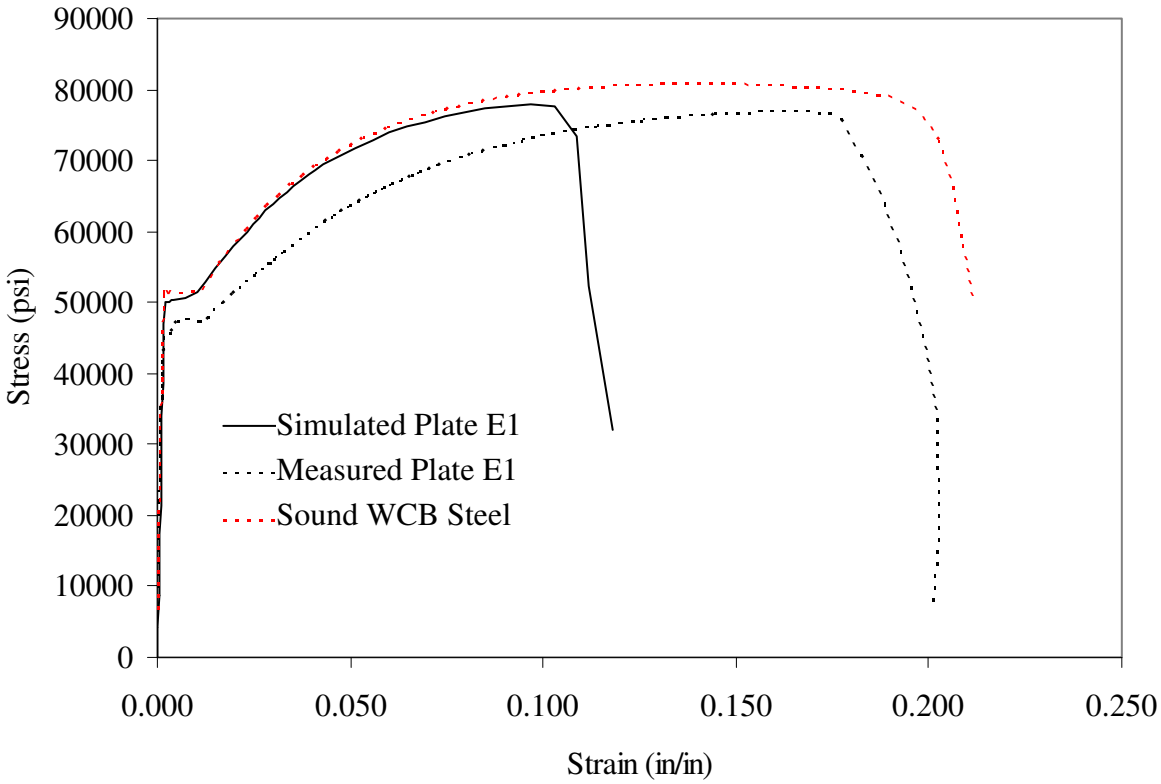

Figure 23 Measured stress-strain curves for sound cast material and plate E1 with porosity are compared to predicted curve for plate E1 using *ABAQUS* with porous metal plasticity model.

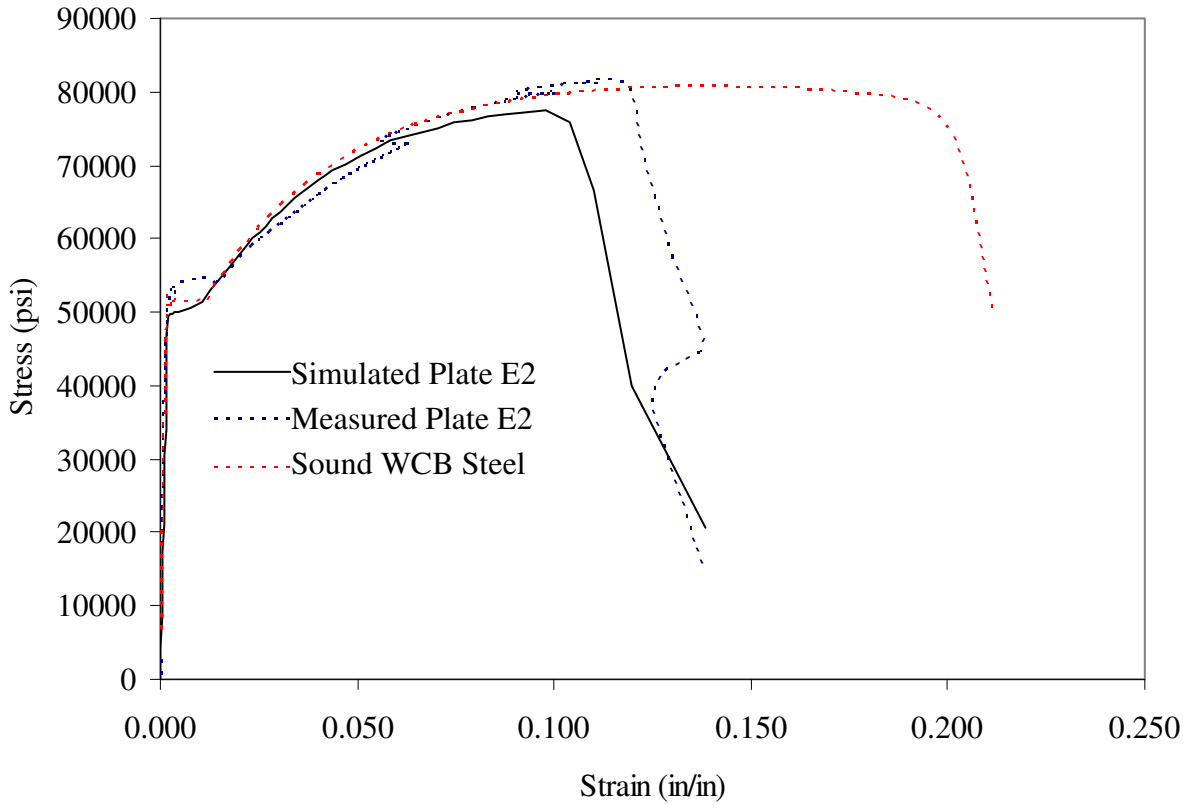

Figure 24 Measured stress-strain curves for sound cast material and plate E2 with porosity are compared to predicted curve for plate E2 using *ABAQUS* with porous metal plasticity model.

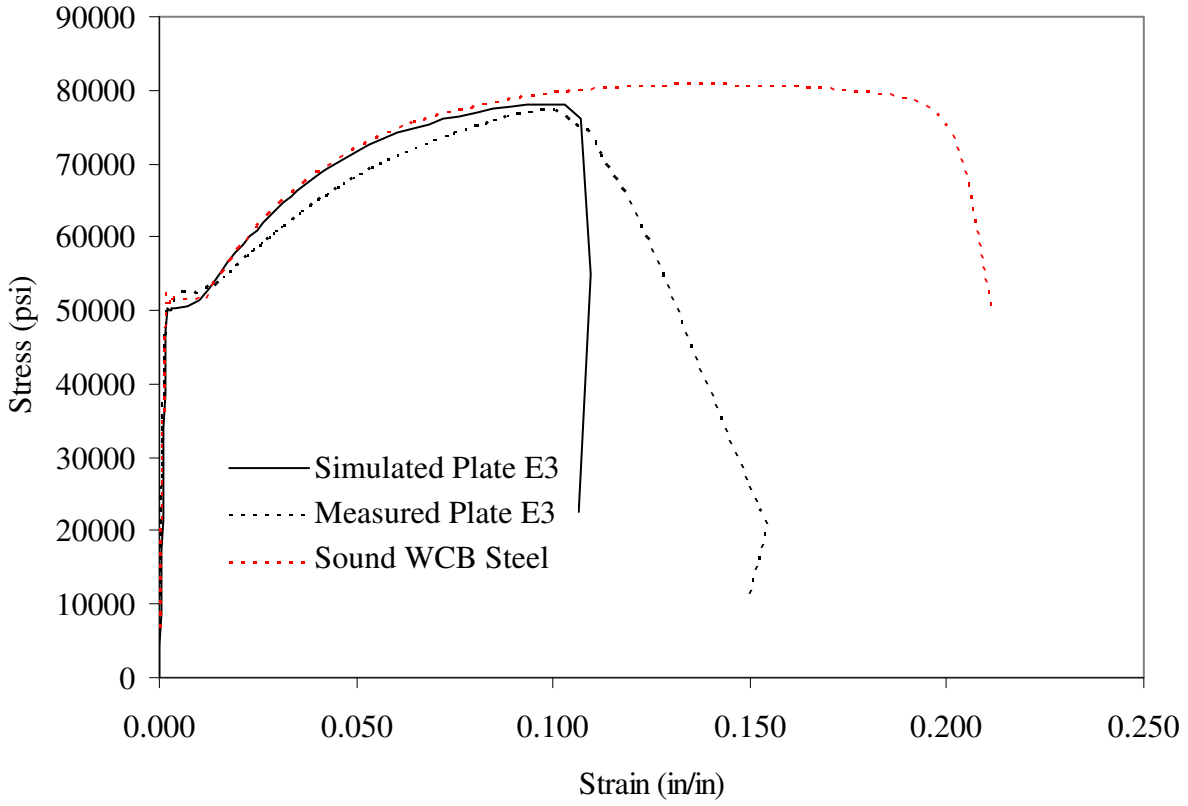

Figure 25 Measured stress-strain curves for sound cast material and plate E3 with porosity are compared to predicted curve for plate E3 using *ABAQUS* with porous metal plasticity model.

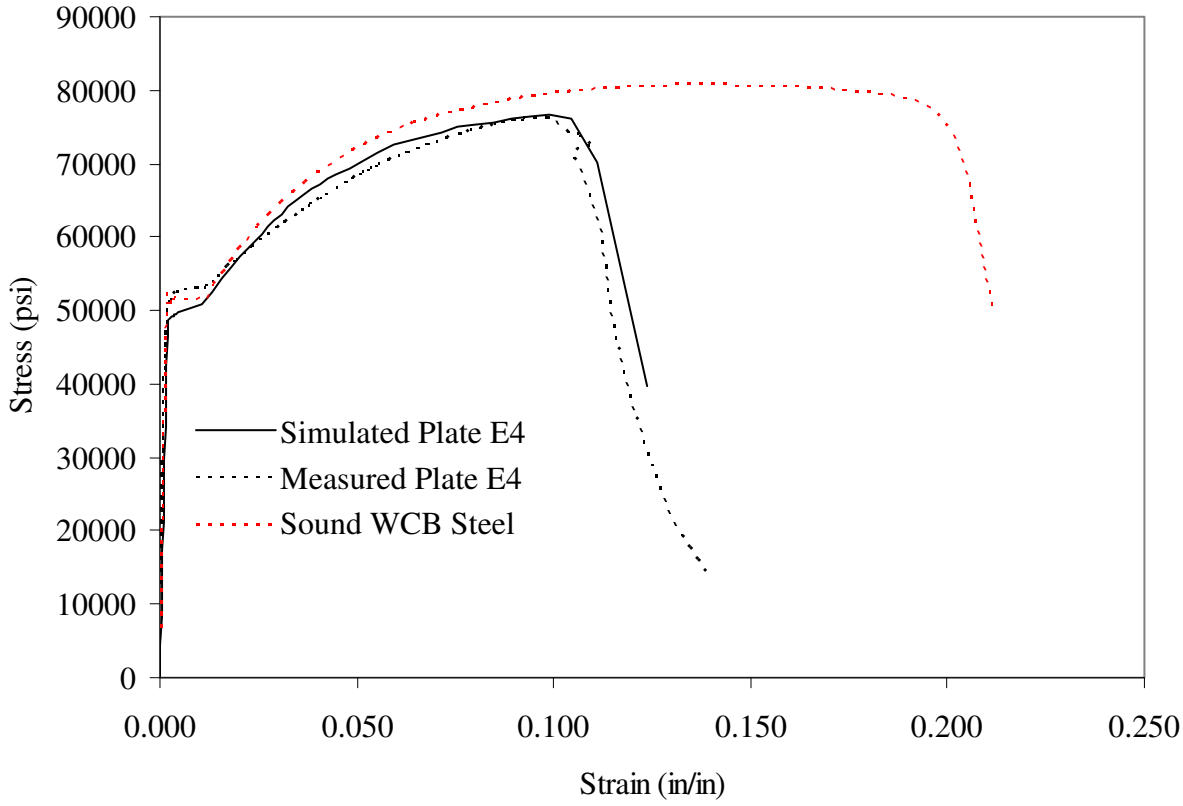

Figure 26 Measured stress-strain curves for sound cast material and plate E4 with porosity are compared to predicted curve for plate E4 using *ABAQUS* with porous metal plasticity model.

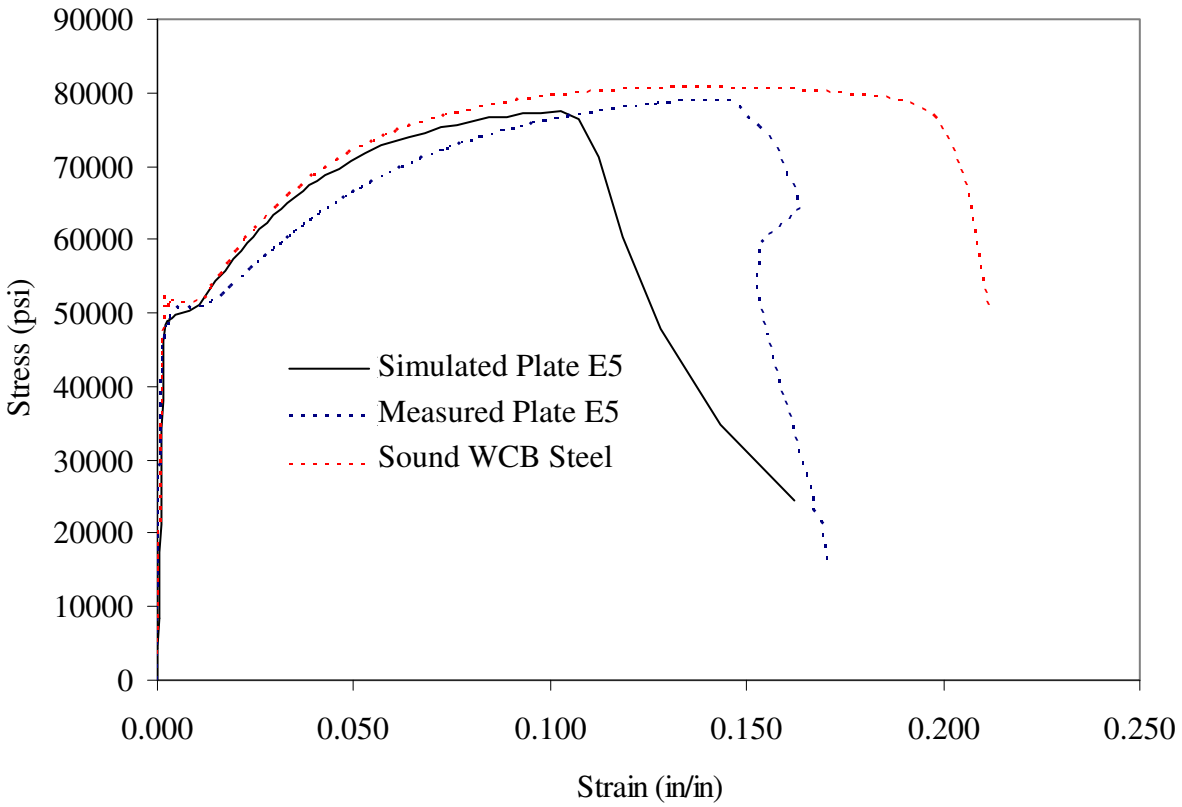

Figure 27 Measured stress-strain curves for sound cast material and plate E5 with porosity are compared to predicted curve for plate E5 using *ABAQUS* with porous metal plasticity model.

Table 3 Measured and predicted plastic property data

	Measured Data			Predicted Data		
Plate ID	Yield Stress 0.2%	UTS	Elongation	Yield Stress 0.2%	UTS	Elongation
	(ksi)	(ksi)	(%)	(ksi)	(ksi)	(%)
D2	55.65	83.05	16	50.8	79.9	16.3
D3	56.35	83.49	16.3	49.8	78.2	15.5
D4	54.39	80.41	12.8	49.5	75.9	11.1
D5	54.15	83.51	17.1	50.3	80.6	17
E1	47.75	78.61	19.6	50.3	77.8	11.8
E2	53.38	81.52	13.8	49.8	77.4	13.9
E3	51.53	77.17	15	51.1	78.1	10.7
E4	52.52	76.24	13.8	49.2	76	12.3
E5	50.65	78.88	17	48.9	77.4	16.2
Sound Data	51.76	80.65	22	50.8	80.6	21.5

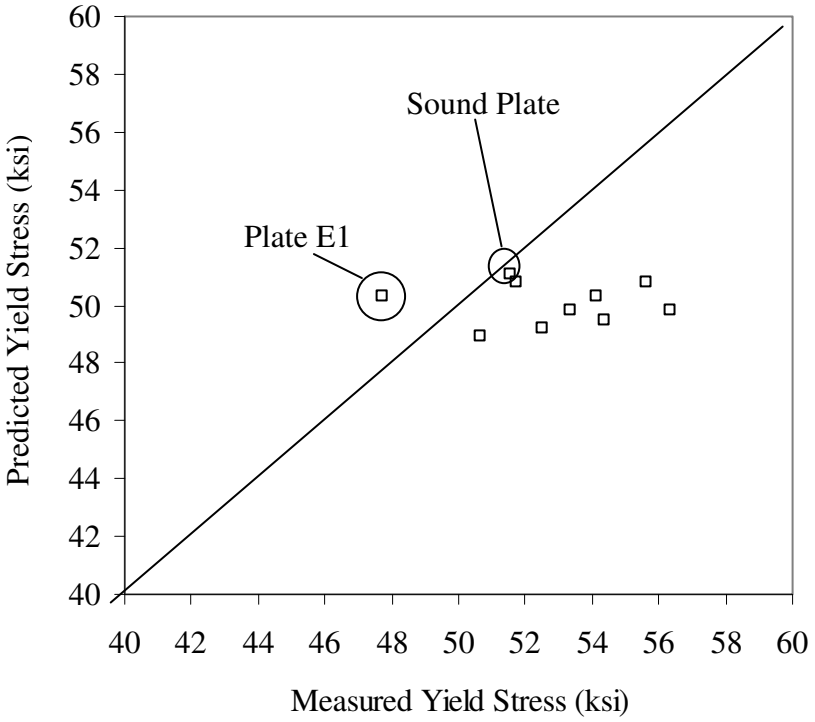

Figure 28 Measured versus predicted yield stress for WCB steel; sound and with porosity.

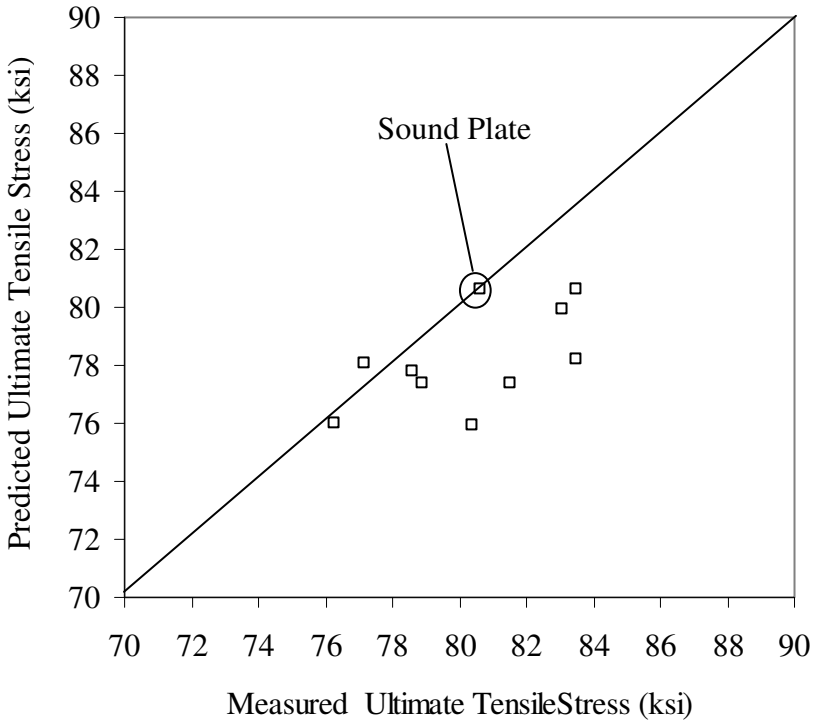

Figure 29 Measured versus predicted ultimate tensile stress for WCB steel; sound and with porosity.

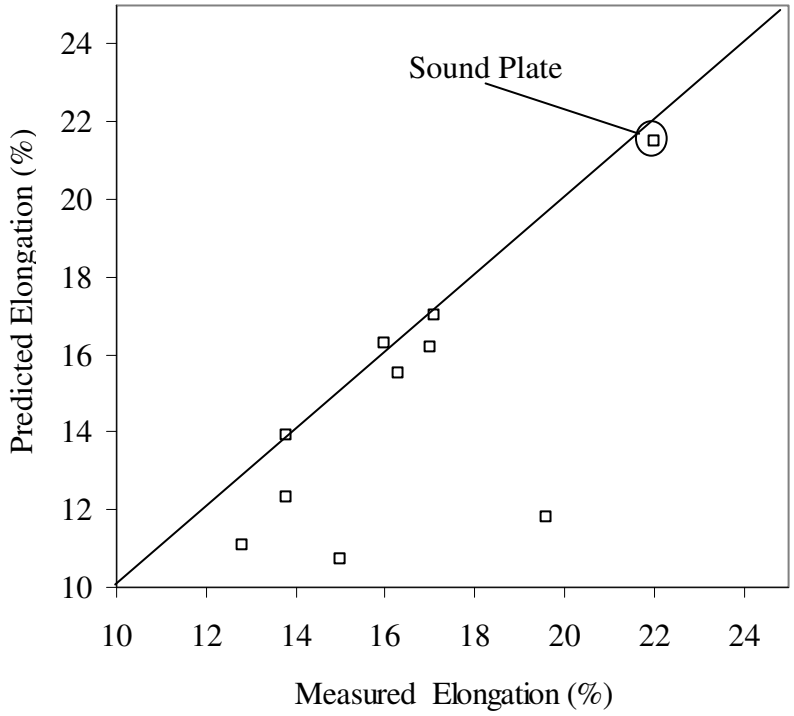

Figure 30 Measured versus predicted percent elongation for WCB steel; sound and with porosity.

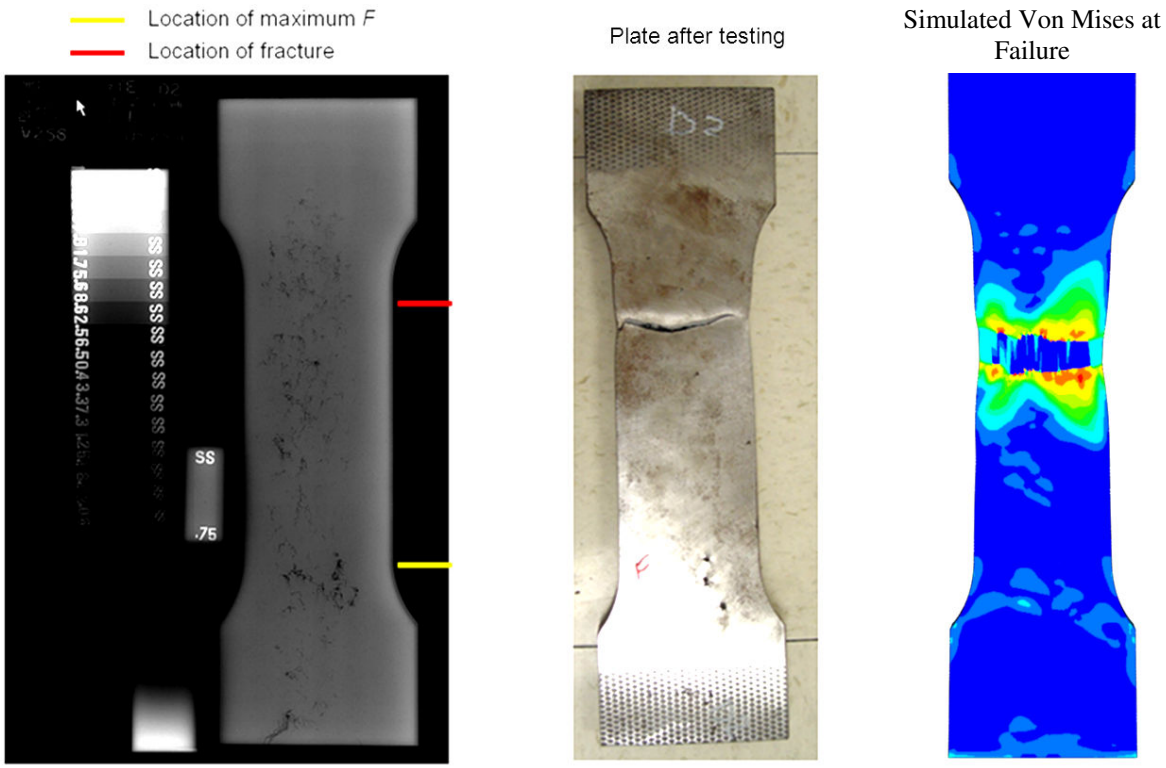

Figure 31 From left to right, radiograph used to determine porosity in plate D2, plate D2 after testing, and plate D2 simulation Von Mises stress at failure.

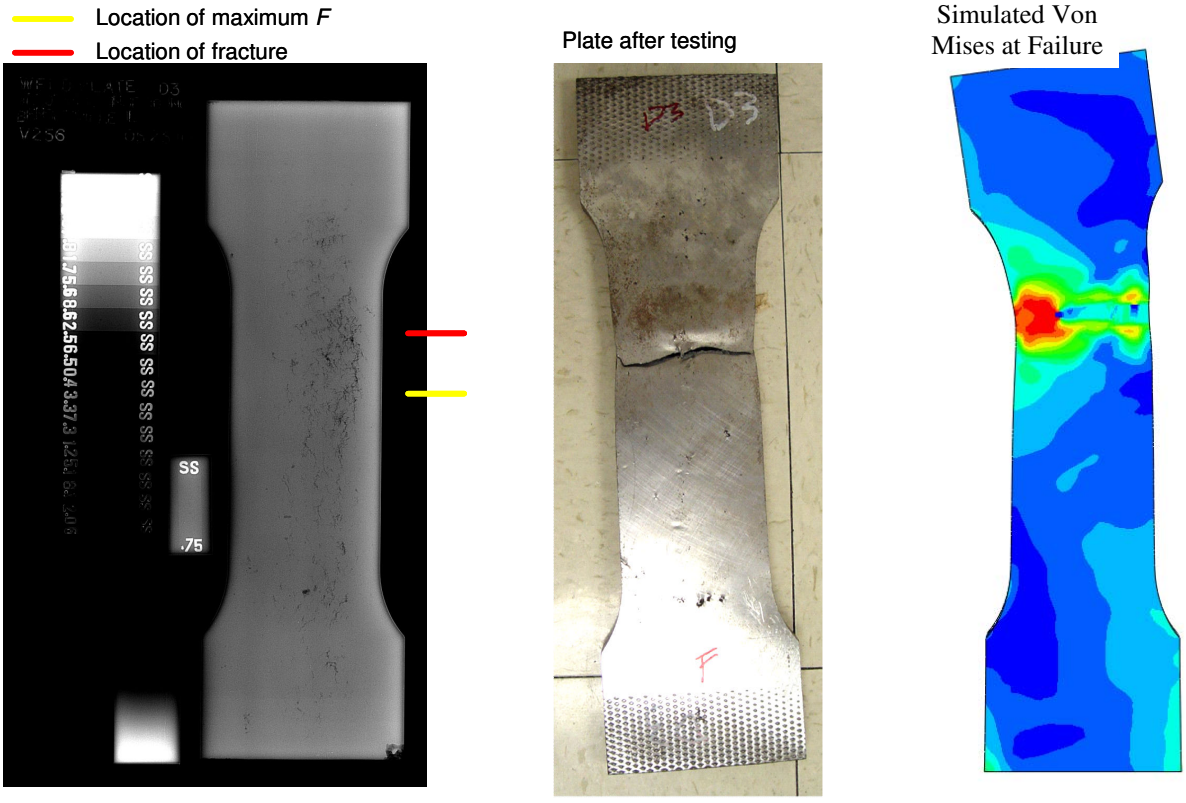

Figure 32 Radiograph used to determine porosity in plate D3, plate D3 after testing, and plate D3 simulation Von Mises stress at failure.

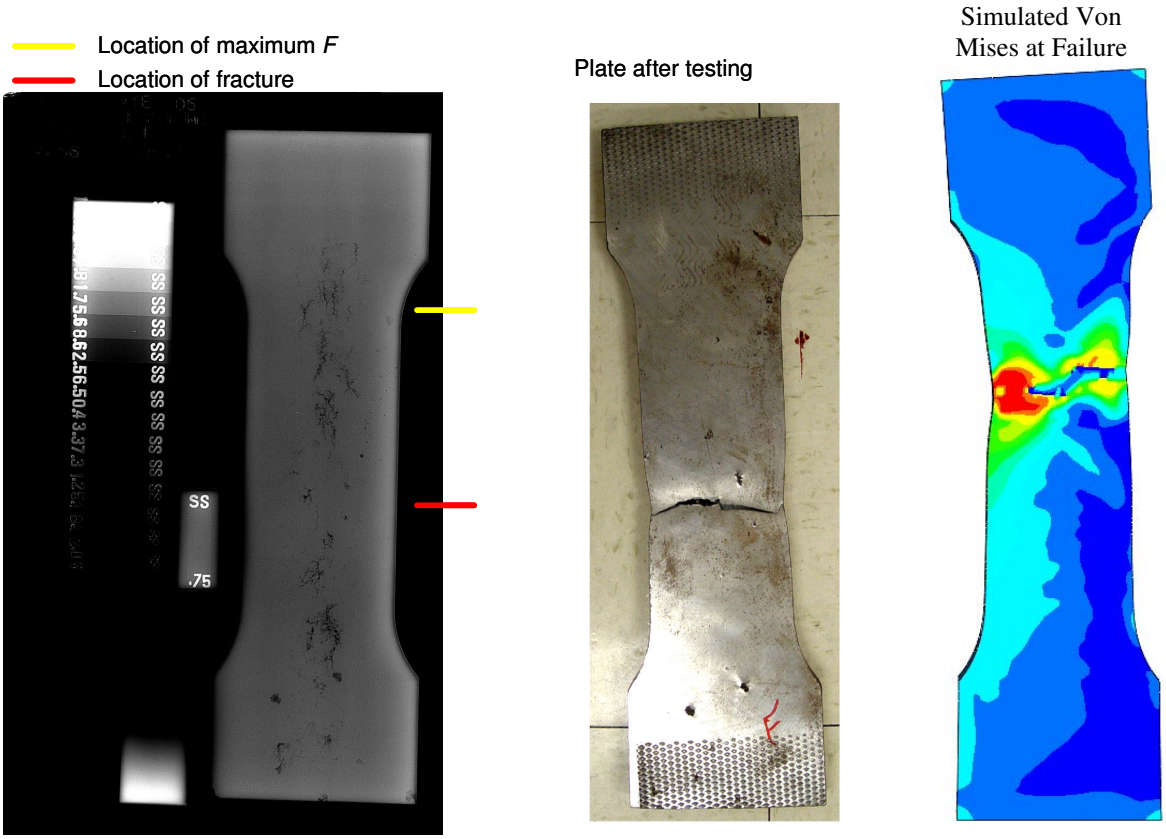

Figure 33 From left to right, radiograph used to determine porosity in plate D5, plate D5 after testing, and plate D5 simulation Von Mises stress at failure.

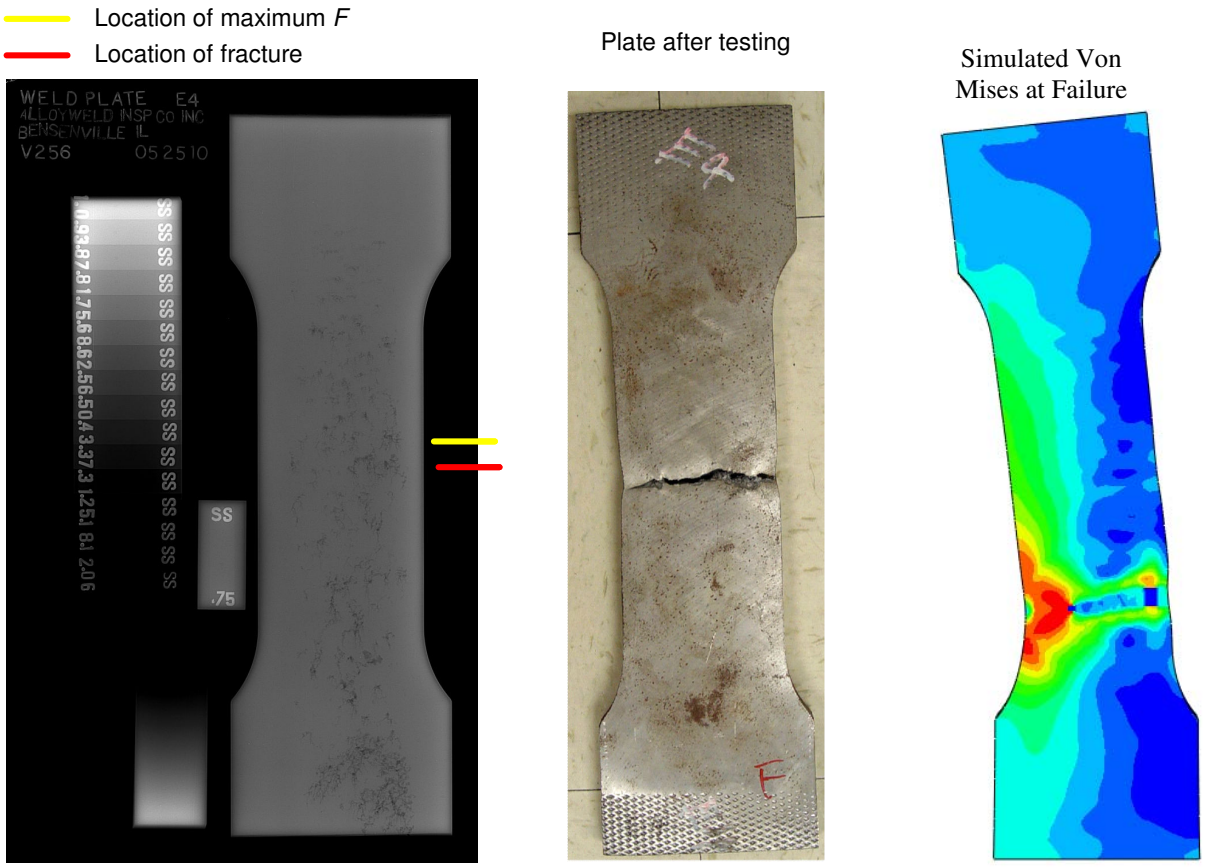

Figure 34 Radiograph used to determine porosity in plate E4, E4 after testing, and E4 simulation at failure.

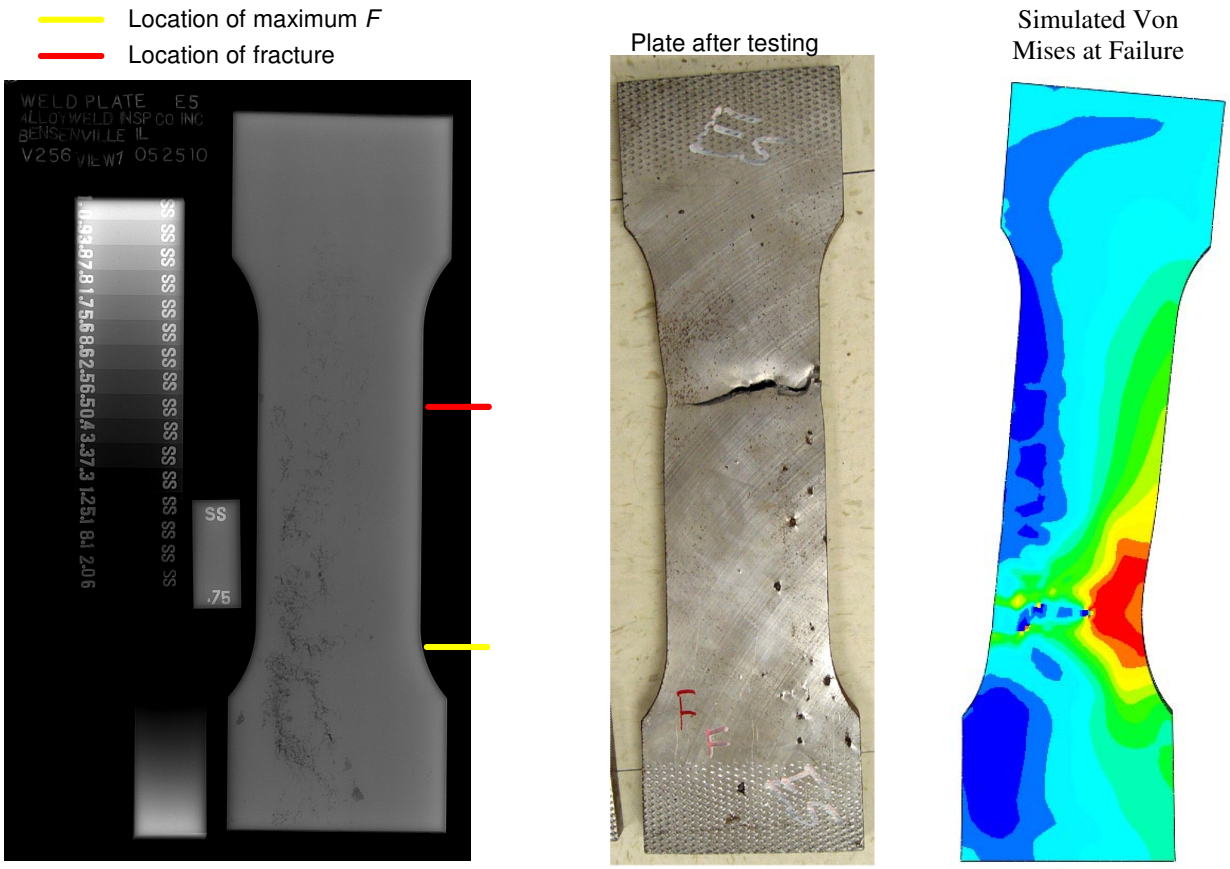

Figure 35 From left to right, radiograph used to determine porosity in plate E5, plate E5 after testing, and plate E5 simulation Von Mises stress at failure.

In Figures 31 to 35 the simulation results for the Von Mises stress on the plate surface at failure on the far right side image in each figure is shown, and from this the predicted failure location is apparent. Sometimes the locations of the measured and predicted failures agree well, and sometimes they do not. In plates D2 and D3, the locations of the simulation and measured failures agree. In Figure 33, it is difficult the see from the radiograph why the failure location is where it is. There do not appear to be indications at the location. In this case, the simulation predicts failure in a region with more porosity on the radiograph. A similar observation is made examining Figure 35 for plate E5, where the failure is predicted at the location of the maximum RT indication, and a region of visible porosity. Yet, the plate E5 fails in a seemingly much sounder region. Note in Figure 35 that the radiograph was taken from the opposite direction from the orientation of the photo of the plate, and the indications on the left hand side of the radiograph are on the right side of the photograph. For plate E4, in Figure 34, the failure location is predicted at a location other than what was observed, but it is a region of noticeable porosity on the radiograph. The failure location for E4 corresponded to the maximum indication from applying the new RT standard.

It is worth examining the simulation of plate E4 in more detail to understand the model and its results better, and to gain insight into the behavior of the failure process for the plates with porosity. The porosity/void fraction, Von Mises stress and plastic strain will be examined for the plate E4 simulations at three points along the stress-strain curve. As shown in Figure 36, results will be examined at points in the curve where the strain is 0.014, 0.045 and 0.104 at Points 1, 2, and 3, respectively. Note that Point 1 is still in the elastic part of the curve, Point 2 is about midway through the plastic region and Point 3 is at the position of UTS just prior to the onset of failure. Only results at the mid-thickness of the plates are discussed since the porosity there determines the overall tensile response and the failure. In Figure 37 the results for porosity fraction are shown. At Point 1 the porosity is virtually unchanged from the initial porosity field (not shown). The scale is set to a maximum porosity fraction of $f = 0.15$ since beyond that point there is no load carrying capacity, and *ABAQUS* ceases calculating it. From Point 1 to 3 note how porosity (or void fraction) "damage" increases until failure occurs at $f = 0.15$. Positions of observed and predicted failure are noted. At Point 3 it is apparent why the simulation predicts failure where it does as there is a connected failed zone there, as discussed regarding Figure 1 (e). However, the location where the plate actually failed shows almost as much damage. Improving the radiographic analysis that determines the porosity field might result in failure at the right location. In Figure 38 the Von Mises stress results at the three points on the curve are presented. Note that even in the elastic range the stress exceeds the yield stress at some locations (the gray areas for Point 1 results). Note that the areas with porosity carry considerably less stress or none at all. There is considerable stress redistribution at the casting mid-thickness. The plastic strain results are shown in Figure 39. Again note that even in the elastic part of the curve there is plastic strain due to, and near to, the porosity. Like the stress, the plastic strain is higher in regions with less porosity that are bearing more stress. The results shown are just for one plate, and one slice at the mid-thickness. Hopefully these results give some additional insight into the model, its results, the complexity of the interaction between the porosity and the elastic-plastic model, and the resulting non-uniform stress and strain fields.

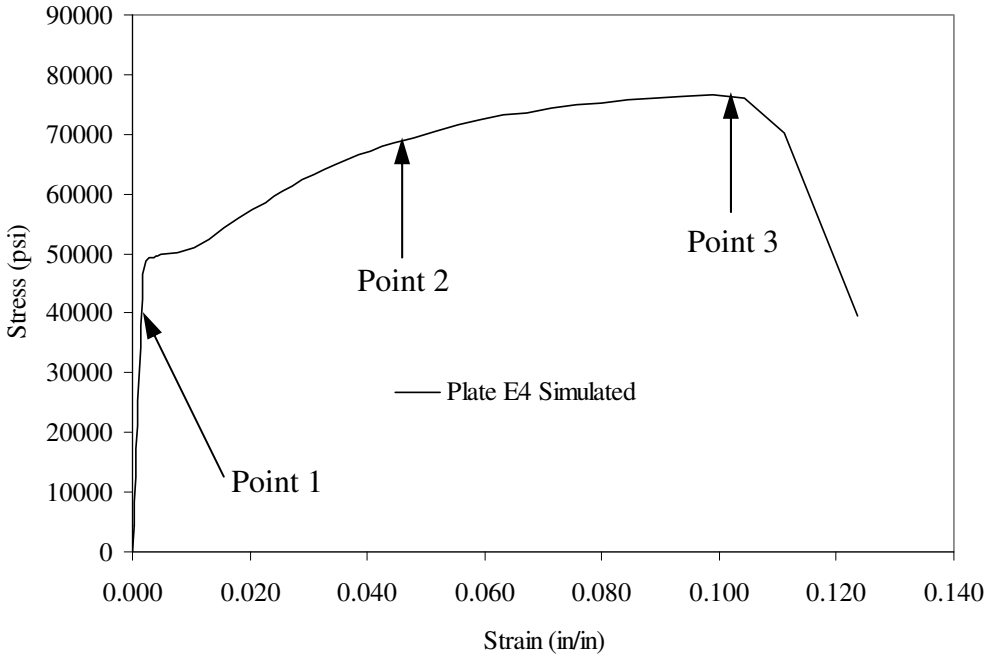

Figure 36 Strain-strain curve from simulation of plate E4 showing the three points in the curve where results at the mid-thickness plane are examined, corresponding to strains 0.014, 0.045 and 0.104.

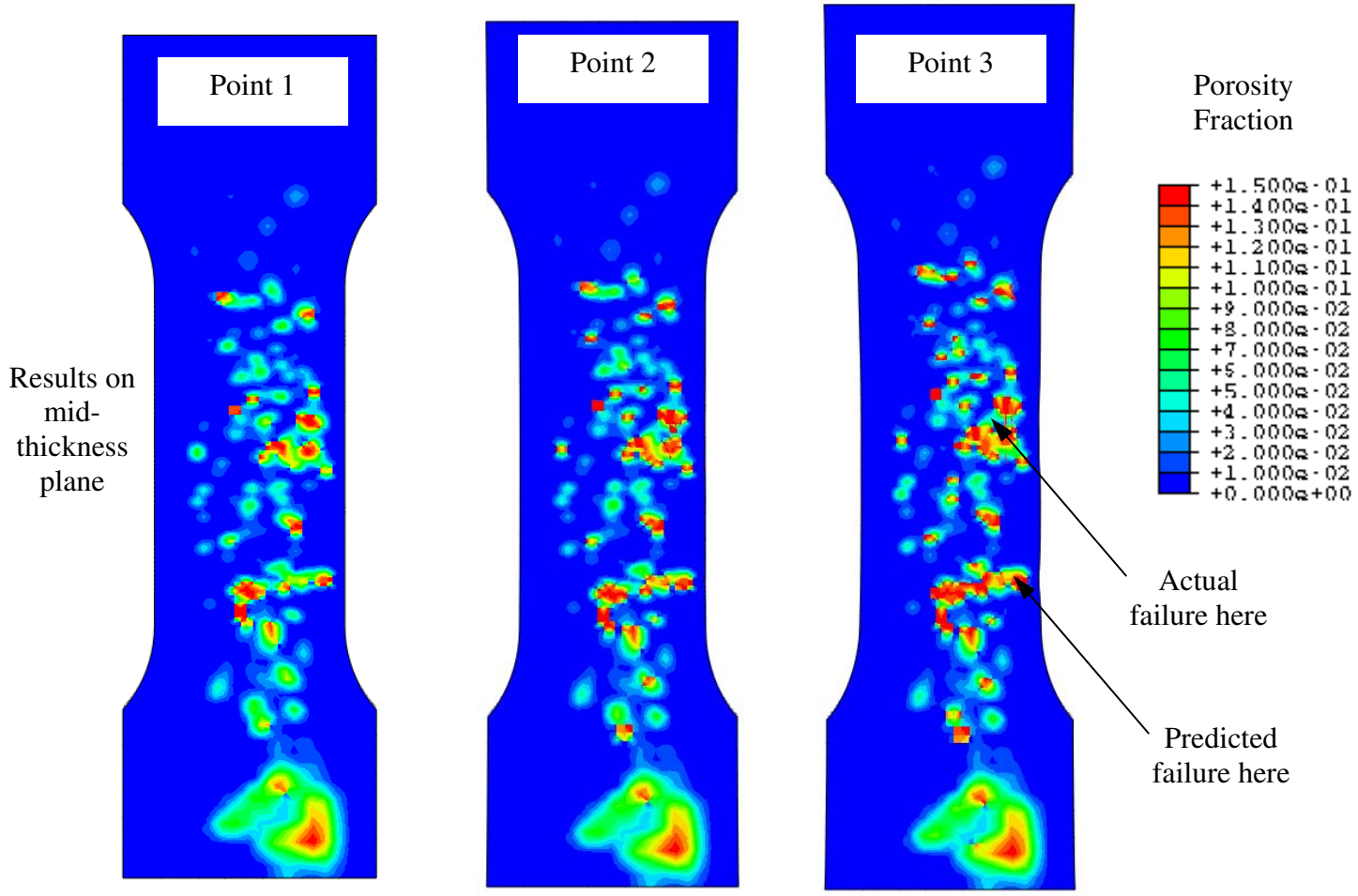

Figure 37 Simulation results for porosity fraction at the plate mid-thickness. Note how porosity (or void fraction) damage increases until failure occurs at $f = 0.15$. Positions of failure also noted.

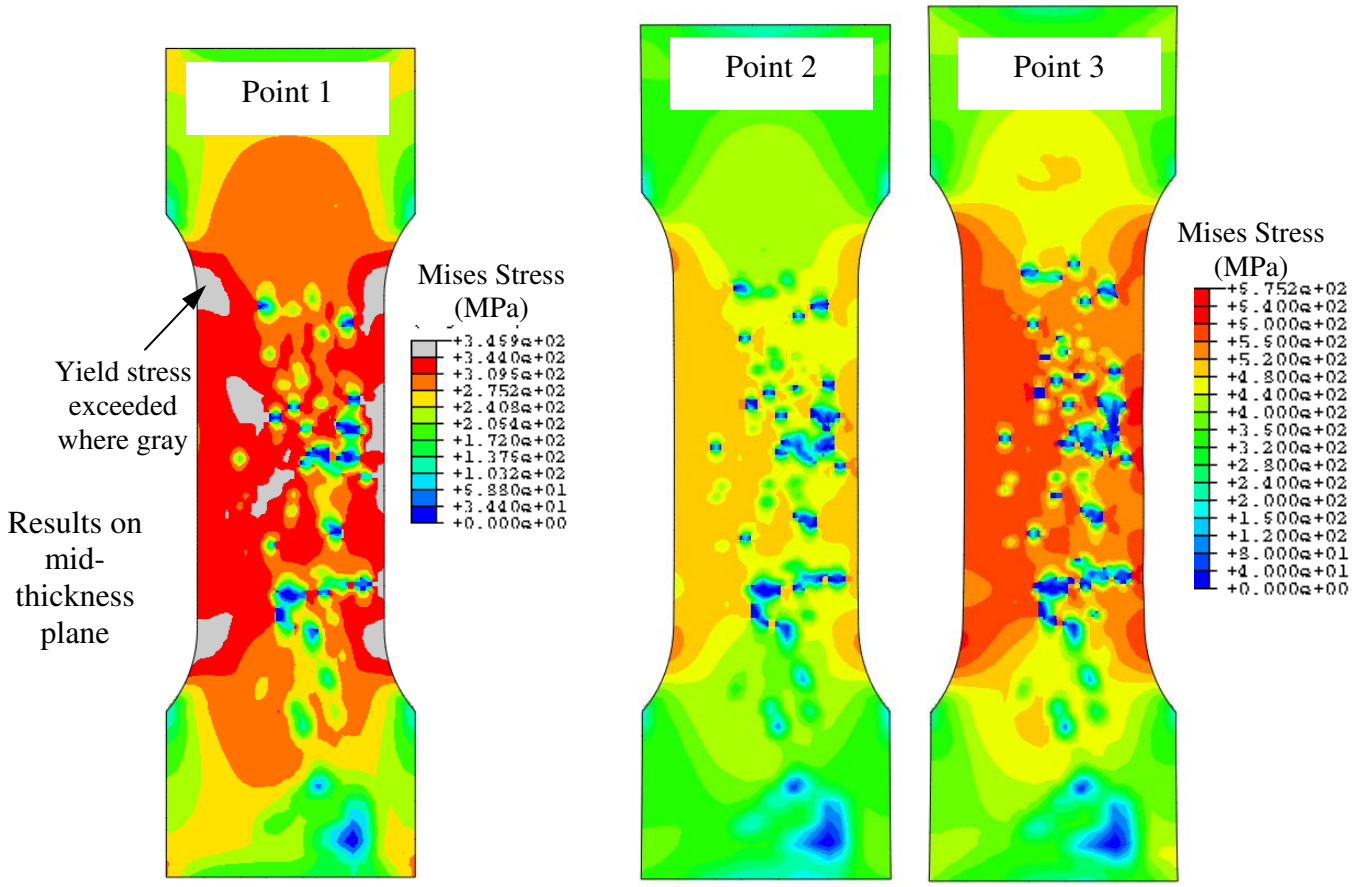

Figure 38 Von Mises stress from simulation at the mid-thickness plane of plate E4. Gray areas denote where yield stress is exceeded for Point 1. Scale at far right is for Points 2 and 3.

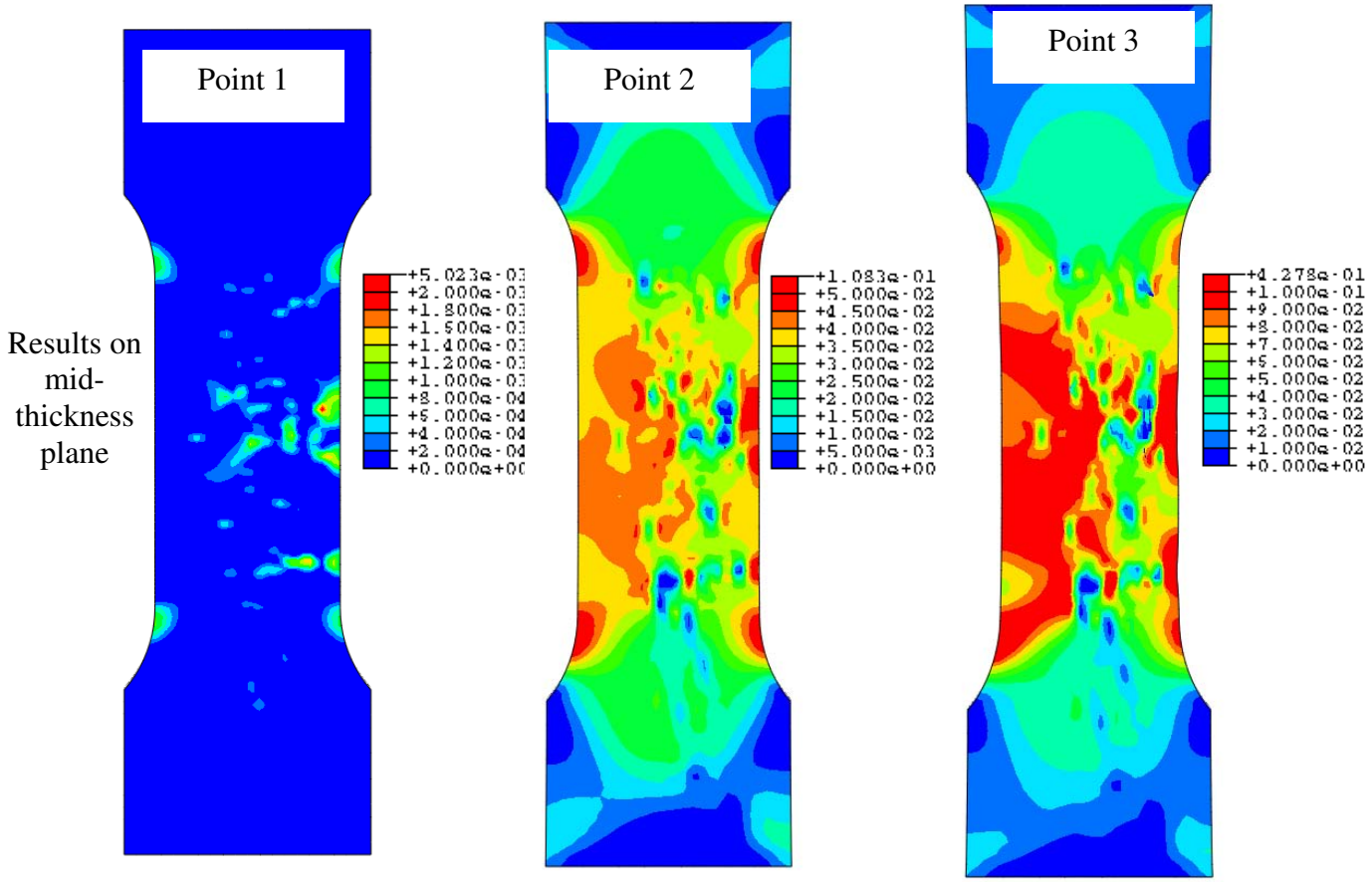

Figure 39 Plastic strain from simulation at the mid-thickness plane of plate E4. Note that the scale is increasing from Point 1 to 3. Note also plastic strain even in the elastic portion for Point 1.

IV. CONCLUSIONS AND RECOMMENDATIONS

The porous metal plasticity model in *ABAQUS* is an often used model to predict elastic-plastic mechanical behavior of porous materials and tensile response to failure. The model requires nine parameters. Here the parameters for WCB steel were determined by consulting the literature for the range of these parameters for ductile metals, and then matching up the measured and predicted stress-strain curves for the sound steel through changing parameters in a trial and error process. Using these model parameters, and porosity fields mapped from the radiographs in finite element models of the castings, tensile testing curves for castings with centerline porosity were simulated. The predicted and measured curves are compared for nine castings, and the simulated castings after failure are compared to the actual failures. In several cases the comparison of the curves is quite good, and the ductility (elongation) responses of the castings with porosity are predicted reasonably well.

Some disagreement remains between prediction and measurement but the overall behavior of the porous casting is correctly predicted using the data from the radiographs. The clearest factors contributing to the disagreement are due to assumptions/limitations in the porous metal plasticity model and assumptions of the how the porosity is distributed at the casting centerline. Nevertheless, this work demonstrates how casting tensile performance in the presence of porosity might be predicted from a radiograph. The authors anticipate improving this work by investigating further how the porosity is distributed through the plate thickness. The failed castings will be radiographed to observe the internal damage by comparing the before- and after-testing radiographs. Selected sections of the plates will also be machined in order to visualize the through thickness porosity distribution. Only by making the porosity distributions used in the simulations more realistic can the accuracy of the model to predict the elastic-plastic response of steel in the presence of porosity truly be determined.

ACKNOWLEDGEMENTS

This research was undertaken through the American Metalcasting Consortium (AMC). AMC is sponsored by Defense Supply Center Philadelphia (DSC, Philadelphia, PA) and the Defense Logistics Agency (DLA, Ft. Belvoir, VA). This work was conducted under the auspices of the Steel Founders' Society of America (SFSA) through substantial in-kind support and guidance from SFSA member foundries. In particular, the authors gratefully appreciate the participation of Sivyer Steel Casting for heat treating the tensile test plates. The valuable tensile test data could not have been acquired without the 800,00 lb force capacity test machine at SSAB North American Division, Muscatine, Iowa. Any opinions, findings, conclusions, or recommendations expressed herein are those of the authors and do not necessarily reflect the views of DSC, DLA, or the SFSA and any of its members.

REFERENCES

1. Anderson, T.L., “Fracture Mechanics: Fundamentals and Applications,” CRC Press, 2005, pp. 219-231.
2. Hardin, R.A., and Beckermann, C., "Simulation of the Mechanical Performance of Cast Steel with Porosity: Static Properties," in Proceedings of the 60th SFSA Technical and Operating Conference, Paper No. 4.3, Steel Founders' Society of America, Chicago, IL, 2006.

3. Hardin, R.A., and Beckermann, C., "Prediction of Fatigue Life of Cast Steel in the Presence of Porosity," in Proceedings of the 61st SFSA Technical and Operating Conference, Paper No. 5.8, Steel Founders' Society of America, Chicago, IL, 2007.
4. P. Heuler, C. Berger, J. Motz, "Fatigue Behaviour of Steel Castings Containing Near-Surface Defects", Fatigue & Fracture of Engineering Materials & Structures, 1992, 16(1), pp. 115-136.
5. Hardin, R. and Beckermann, C., "Effect of Porosity on Mechanical Properties of 8630 Cast Steel," in Proceedings of the 58th Technical and Operating Conference, SFSA, Chicago (2004).
6. Sigl, K.M., Hardin, R., Stephens, R.I., and Beckermann, C., "Fatigue of 8630 Cast Steel in the Presence of Shrinkage Porosity," in Proceedings of the 57th Technical and Operating Conference, SFSA, Chicago (2003).
7. K.M. Sigl, R. Hardin, R.I. Stephens, and C. Beckermann, "Fatigue of 8630 Cast Steel in the Presence of Porosity," International Journal of Cast Metals Research, 2004, 17(3), pp. 130-146.
8. Herakovich, C.T., and Baxter, S.C., "Influence of Pore Geometry on the Effective Response of Porous Media," Journal of Materials Science, 1999, 34, pp.1595-1609.
9. Roberts, A.P., and Garboczi, E.J., "Elastic Properties of Model Porous Ceramics," J. Am. Ceram. Soc., 2000, 83(12). pp. 3041-3048.
10. Ramakrishnan, N. and Arunachalam, V.S., "Effective Elastic Moduli of Ceramic Materials," J. Am. Ceram. Soc., 1993, 76(11), pp. 2745–2752.
11. Zhang E. and Wang B., "On the Compressive Behavior of Sintered Porous Coppers with Low to Medium Porosities – Part I: Experimental Study," Int. Journal of Mechanical Sciences, 2005, 47, pp. 744-756.
12. Dewey, J.M., "The Elastic Constants of Materials Loaded with Non-rigid Fillers," Journal of Applied Physics, 1947, 18, pp. 578-581.
13. Gurson, A.L., "Continuum Theory of Ductile Rupture by Void Nucleation and Growth: Part I — Yield Criteria and Flow Rules for Porous Ductile Materials," Journal of Engineering Materials and Technology, 1977, 99, pp. 2–15.
14. Tvergaard, V., "Influence of Voids on Shear Band Instabilities under Plane Strain Condition," International Journal of Fracture Mechanics, 1981, 17, pp. 389–407.
15. Needleman, A. and Tvergaard, V. "An Analysis of Ductile Rupture in Notched Bars," J. Mech. Phys. Solids, 1984, 32, pp. 461–490.
16. Dassault Systèmes, ABAQUS Theory Manual, Version 6.10, 2010, section 4.3.6 Porous Metal Plasticity.
17. Hardin, R.A., and Beckermann, C., "Effect of Porosity on the Stiffness of Cast Steel," Metall. Mater. Trans. A, Vol. 38A, 2007, pp. 2992-3006.
18. Hardin, R.A., and Beckermann, C., "Validation and Gage R&R Studies of a New Radiography Standard for Steel Castings," in Proceedings of the 64th SFSA Technical and Operating Conference, Paper No. 2.6, Steel Founders' Society of America, Chicago, IL, 2010.
19. ASM, *Tensile Testing*, 2nd Ed., Edited by J.R. Davis, ASM International, Materials Park, OH, 2003, p. 43